Statistical Modeling of MIMO Mobile-to-Mobile Underwater Channels

Alenka G. Zajić, *Member, IEEE*

***Abstract*— This paper proposes a geometry-based statistical model for wideband multiple-input multiple-output (MIMO) mobile-to-mobile (M-to-M) shallow water acoustic (SWA) multipath fading channels. From the reference model, the corresponding MIMO time-frequency correlation function, Doppler power spectral density, and delay cross-power spectral density are derived. These statistics are important tools for design and performance analysis of MIMO M-to-M SWA communication and sonar systems. Finally, the derived statistics are compared with the experimentally obtained channel statistics and close agreement is observed.**

***Index Terms*— Shallow water acoustic channels, mobile-to-mobile underwater channels, multiple-input multiple-output underwater channels, wideband channels, synthetic aperture sonar, underwater sensor networks.**

I. Introduction

There has been a growing interest in designing underwater wireless sensor networks because of their ability to bring computation and sensing into the underwater environment. Underwater networks have many potential applications, including seismic monitoring, scientific exploration of the ocean, tactical surveillance, pollution monitoring, offshore exploration, and support for underwater robots. To make these applications feasible, there is a need for wireless underwater acoustic communications among deployed sensors and autonomous underwater vehicles. Statistical characterization of the acoustic communication channel is necessary in order to assess system performance and develop methods to improve the quality of a communication system [1]. These results can also be used to improve the performance of sonar systems [2], [3].

The shallow water acoustic (SWA) channel is one of the most challenging communication channels because it suffers the path-dependent Doppler and angle spreading, which results in a time-varying wideband channel impulse response with long delay spreads [4], [5]. While there exist several deterministic and statistical simulation models for SWA channels [6]-[11], a statistical framework for SWA channels, i.e., correlation functions, Doppler power spectral density, delay cross-power spectral density, etc., is still an open problem. These statistics are necessary tools for a proper design and analysis of multiple-input multiple-output (MIMO) mobile-to-mobile (M-to-M) SWA communication or sonar systems. Furthermore, the closed-form expressions of these statistics can be useful for estimation of physical parameters such as angle spread, mean angles of departure and arrival, etc. Abdi and Guo [12] were the first to derive the frequency correlation function for *time-invariant* stationary SWA channels, by taking into account only macro-scattering effects.

In contrast, this paper models a *time-varying* MIMO M-to-M SWA channel by taking into account both, the macro- and micro-scattering effects. We first introduce a new geometry-based statistical model for wideband MIMO M-to-M SWA multipath fading channels. The proposed model characterizes the sound propagation in shallow water isovelocity environments by combining the deterministic ray-tracing theory with the statistical methods needed to characterize the random components of the propagation medium. From the statistical model, the corresponding MIMO time-frequency correlation function (tf-cf), MIMO Doppler power spectral density (D-psd), and MIMO delay cross-power spectral density (dc-psd) for a shallow water isovelocity environment are derived. Finally, to illustrate the utility of the proposed model, we compare the correlation functions, D-psd, and dc-psd with those obtained from the measurements in [13], [14]. The results show close agreement between the derived and measured channel statistics. Furthermore, they show that the proposed model outperforms the models in [12] and [14].

The remainder of the paper is organized as follows. Section II introduces the geometry-based statistical model for wideband MIMO M-to-M SWA multipath fading channels. Section III derives the MIMO tf-cf, the D-psd, and the dc-psd for a shallow water isovelocity environment. Section IV compares the analytical and measured results for the tf-cf, the D-psd, and the dc-psd. Finally, Section V provides some concluding remarks.

II. Geometry-based Statistical Model for MIMO M-to-M SWA Channels

This paper considers a medium or long range MIMO communication system with L_t transmit and L_r receive transducers. The propagation occurs in shallow water environments with constant sound speed, i.e., sound energy propagates along the plane waves. The propagation is characterized with either line-of-sight (LoS) or non-line-of-sight (NLoS) conditions between the transmitter ($\mathrm{T_x}$) and the receiver ($\mathrm{R_x}$). The MIMO M-to-M SWA channel can be described by an $L_r \times L_t$ matrix $\mathbf{H}(t,\tau) = [h_{ij}(t,\tau)]_{L_r \times L_t}$ of the input-delay spread functions.

Fig. 1 depicts LoS path and several macro-eigenrays travelling between the $\mathrm{T_x}$ and $\mathrm{R_x}$ in a SWA channel with $L_t =$

Paper approved by Prof. Michel Yacoub, the Associate Editor for IEEE Transactions on Vehicular Technology. Manuscript received April 23, 2010; revised November 11, 2010; revised February 18, 2011.

Alenka G. Zajić is with the School of Computer Science, Georgia Inst. of Tech., Atlanta, GA 30332 USA

$L_r = 1$ transducer elements. The SWA channel is modeled as a two-dimensional (2-D) waveguide bounded from the top and bottom. The surface and bottom boundaries reflect an acoustic signal, which results in multiple macro-eigenrays travelling between the $\mathrm{T_x}$ and $\mathrm{R_x}$, as shown in Fig. 1. At any time instance t, the $\mathrm{R_x}$ receives $2S$ downward arriving (DA) macro-eigenrays (i.e., the last reflection is from the surface), each one having different number of s surface and $\hat{b}$ bottom reflections, where S denotes the maximum number of interactions between any DA macro-eigenray and the surface, $1 \leq s \leq S$, and $s-1 \leq \hat{b} \leq s$. For example, if a DA macro-eigenray has only one interaction with the surface, i.e., $S = 1$, there are two possible paths that this eigenray travelled. The first path is a single-bounced path, where a DA macro-eigenray started upwards, interacted with the surface, and arrived at the $\mathrm{R_x}$, i.e., $s = 1, \hat{b} = 0$. The second path is a double-bounced path, where a DA macro-eigenray started downwards, interacted with the bottom, then interacted with the surface, and arrived at the $\mathrm{R_x}$, i.e., $s = 1, \hat{b} = 1$. Note that for $S = 1$, both macro-eigenrays will reach the $\mathrm{R_x}$ because they have similar energy [11], [15]. Similarly, there are $2B$ upward arriving (UA) macro-eigenrays (i.e., the last reflection is from the bottom) with b bottom and $\hat{s}$ surface reflections, where B denotes the maximum number of interactions between a UA macro-eigenray and the bottom, $1 \leq b \leq B$ and $b-1 \leq \hat{s} \leq b$. In contrast to fixed-to-mobile cellular radio channels, where single-bounced eigenrays are dominant [16], [17], in SWA channels, the energy stays trapped in the waveguide and the number of bounces (i.e., interactions with the surface and bottom) can be large [15]. However, the experimental results for medium and long range SWA channels show that the number of different macro-eigenrays that arrive at the $\mathrm{R_x}$ rarely exceeds 8 i.e., $2S + 2B = 8$ [11], [13], [14].

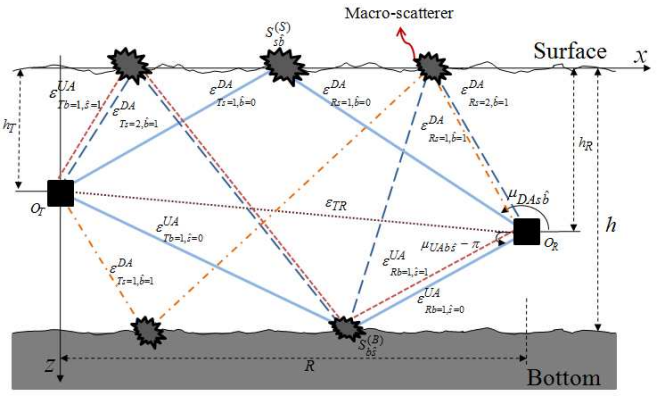

Fig. 1. Illustration of LoS path and several macro-eigenrays travelling between the $\mathrm{T_x}$ and $\mathrm{R_x}$ in a SWA channel with $L_t = L_r = 1$ transducer elements.

Here we note that the exact positions of scatterers depend on the surface and bottom characteristics and may vary from one location to another and from one time instance to another. The roughness of sea surface and sea bottom is characterized by *micro-scatterers*, as shown in Fig. 2. On the other hand, the locations of *macro-scatterers* depend only on the waveguide geometry and the number of macro-eigenrays, and can be computed [15]. In other words, associated with each of the deterministic macro-eigenrays, there are random signal fluctuations (micro-eigenrays), which account for the time variability of the channel response [9], [15]. To implement this propagation mechanism, each DA macro-eigenray is modeled as an average of $N_{s\hat{b}}$ DA micro-eigenrays. Similarly, each UA macro-eigenray is modeled as an average of $M_{b\hat{s}}$ UA micro-eigenrays. Note that the possible positions of micro-scatterers are clustered around the positions of macro-scatterers, as shown in Fig. 2. This is in contrast to radio channel propagation, where scatterers can be randomly placed anywhere in a 2-D or 3-D plane.

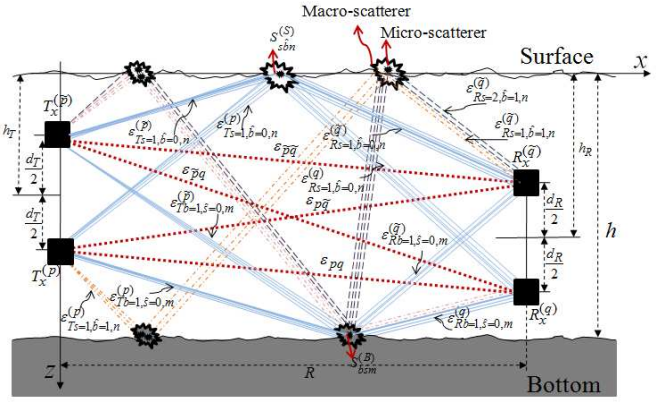

Fig. 2. The geometry-based model for wideband MIMO M-to-M SWA channels with $L_t = L_r = 2$ transducer elements. Each macro-eigenray is represented as a large number of micro-eigenrays.

Fig. 2 shows a SWA channel with $L_t = L_r = 2$ transducer elements. This elementary 2×2 transducer configuration will be used later to construct uniform linear arrays with an arbitrary number of transducer elements. The horizontal spacing between the $\mathrm{T_x}$ and $\mathrm{R_x}$ is denoted by R. The water depth is denoted by h, while the depths of $\mathrm{T_x}$ and $\mathrm{R_x}$ are denoted by h_T and h_R, respectively. As we are interested in medium and long range shallow water communications, we assume that the depths h, h_T, and h_R are much smaller than the distance R. The spacing between two adjacent transducer elements at the $\mathrm{T_x}$ and $\mathrm{R_x}$ is d_T and d_R, respectively. It is assumed that d_T and d_R are much smaller than the depths h, h_T, and h_R. The symbols $\epsilon^{(p)}_{Ts\hat{b}n}$ and $\epsilon^{(p)}_{Tb\hat{s}m}$ denote distances $T^{(p)}_x$-$S^{(S)}_{s\hat{b}n}$ and $T^{(p)}_x$-$S^{(B)}_{b\hat{s}m}$, respectively, where $S^{(S)}_{s\hat{b}n}$ and $S^{(B)}_{b\hat{s}m}$ denote the n^{th} and m^{th} micro-scatterers located around the macro-scatterers $S^{(S)}_{s\hat{b}}$ and $S^{(B)}_{b\hat{s}}$ at the surface and bottom, respectively, for $1 \leq n \leq N_{s\hat{b}}$ and $1 \leq m \leq M_{b\hat{s}}$, as shown in Fig. 2. Similarly, the symbols $\epsilon^{(\tilde{p})}_{Ts\hat{b}n}$, $\epsilon^{(\tilde{p})}_{Tb\hat{s}m}$, $\epsilon^{(q)}_{Rs\hat{b}n}$, $\epsilon^{(q)}_{Rb\hat{s}m}$, $\epsilon^{(\tilde{q})}_{Rs\hat{b}n}$, $\epsilon^{(\tilde{q})}_{Rb\hat{s}m}$, ϵ_{pq}, $\epsilon_{\tilde{p}q}$, $\epsilon_{p\tilde{q}}$, and $\epsilon_{\tilde{p}\tilde{q}}$ denote distances $T^{(\tilde{p})}_x$-$S^{(S)}_{s\hat{b}n}$, $T^{(\tilde{p})}_x$-$S^{(B)}_{b\hat{s}m}$, $S^{(S)}_{s\hat{b}n}$-$R^{(q)}_x$, $S^{(B)}_{b\hat{s}m}$-$R^{(q)}_x$, $S^{(S)}_{s\hat{b}n}$-$R^{(\tilde{q})}_x$, $S^{(B)}_{b\hat{s}m}$-$R^{(\tilde{q})}_x$, $T^{(p)}_x$-$R^{(q)}_x$, $T^{(\tilde{p})}_x$-$R^{(q)}_x$, $T^{(p)}_x$-$R^{(\tilde{q})}_x$, and $T^{(\tilde{p})}_x$-$R^{(\tilde{q})}_x$, respectively. For ease of reference, Fig. 3 details the geometry of the LoS path as well as the geometry of single-bounced surface and single-bounced bottom micro-eigenrays (i.e., $s = 1, \hat{b} = 0$, $b = 1, \hat{s} = 0$) scattered from the $S^{(S)}_{s=1,\hat{b}=0,n}$-th and $S^{(B)}_{b=1,\hat{s}=0,m}$-th micro-scatterers, respectively. The geometry of multiple-bounced micro-eigenrays is similarly defined, but omitted from Fig. 3 for ease of reference. Angles θ_T and θ_R in Fig. 3 describe

the orientations of $\mathrm{T_x}$ and $\mathrm{R_x}$ transducer arrays in the x-z plane, respectively, relative to the x-axis. The $\mathrm{T_x}$ and $\mathrm{R_x}$ are moving with constant speeds v_T and v_R in directions described by angles γ_T and γ_R in the x-z plane (relative to the x-axis), respectively. The symbols $\alpha^{(p)}_{Ts\hat{b}n}$ and $\alpha^{(p)}_{Tb\hat{s}m}$ are the angles of departure (AoD) of micro-eigenrays that start from $T^{(p)}_x$ and impinge on the scatterers $S^{(S)}_{s\hat{b}n}$ and $S^{(B)}_{b\hat{s}m}$, respectively, whereas $\alpha^{(q)}_{Rs\hat{b}n}$ and $\alpha^{(q)}_{Rb\hat{s}m}$ are the angles of arrival (AoA) of the micro-eigenrays scattered from $S^{(S)}_{s\hat{b}n}$ and $S^{(B)}_{b\hat{s}m}$ and arriving at $R^{(q)}_x$, respectively. Finally, the symbols α_{TR} and ϵ_{TR} denote the AoA of LoS ray and the distance O_T-O_R, respectively. For ease of reference, the parameters defined in Figs. 1 - 3 are summarized in Table I.

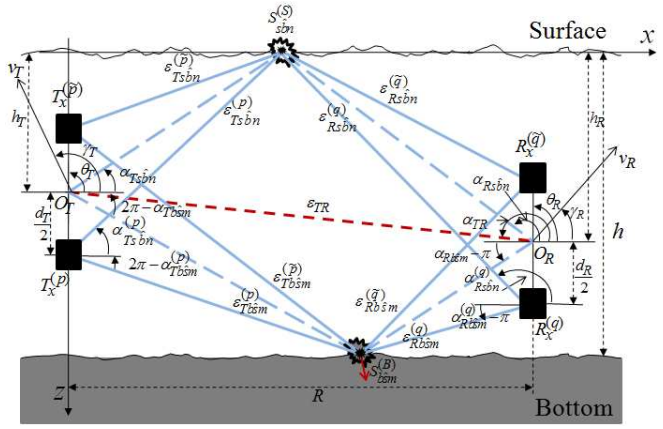

Fig. 3. The detailed geometry of the LoS path, single-bounced surface and single-bounced bottom micro-eigenrays scattered from the $S^{(S)}_{s,\hat{b},n}$ and $S^{(B)}_{b,\hat{s},m}$ micro-scatterers, respectively.

Observe from the geometrical model in Fig. 2 that propagation through SWA channel can be characterized as a superposition of surface-bottom bounced macro-eigenrays and the LoS path between the $\mathrm{T_x}$ and $\mathrm{R_x}$. The macro-eigenrays can be grouped into the UA macro-eigenrays (i.e., the last reflection is from the bottom) and the DA macro-eigenrays (i.e., the last reflection is from the surface). Furthermore, each DA macro-eigenray is represented as an average of $N_{s\hat{b}}$ DA micro-eigenrays, while each UA macro-eigenray is represented as an average of $M_{b\hat{s}}$ UA micro-eigenrays. Then, the input delay-spread function of the pressure link $T^{(p)}_x$-$R^{(q)}_x$ can be written as a superposition of the LoS, UA, and DA macro-eigenrays, viz.

$$h_{pq}(t,\tau) \;=\; h^{LoS}_{pq}(t,\tau) + h^{UA}_{pq}(t,\tau) + h^{DA}_{pq}(t,\tau). \quad (1)$$

The LoS component of the input delay-spread function is

$$h^{LoS}_{pq}(t,\tau) = \sqrt{\frac{K}{K+1}}\sqrt{G_p\left(\alpha_{TR}+\pi\right)G_q\left(\alpha_{TR}\right)}\; L_S(\epsilon_{TR})L_A(\epsilon_{TR})\delta\left(\tau-\tau^{(p,q)}_{TR}(t)\right), \quad (2)$$

where $G_p(\cdot)$ and $G_q(\cdot)$ denote the radiation patterns of the p^{th} transmit and q^{th} receive transducer element, respectively, K is the Rice factor (ratio of LoS to scatter received power), $L_S(\epsilon_{TR})$ and $L_A(\epsilon_{TR})$ denote the propagation loss due to spherical spreading and absorption, respectively, and $\delta(\cdot)$ denotes the Dirac impulse function. The LoS time delay $\tau^{(p,q)}_{TR}(t)$ denotes the travel time of the LoS path, i.e.,

$$\begin{aligned}\tau^{(p,q)}_{TR}(t) \;&=\; \frac{\epsilon_{pq}}{c} + \frac{v_T}{c}t\cos(\alpha_{TR}+\pi-\gamma_T)\\ &+\; \frac{v_R}{c}t\cos(\alpha_{TR}-\gamma_R), \end{aligned}\quad (3)$$

where c is the speed of sound. We assume that the $\mathrm{T_x}$ has omnidirectional transducer elements and therefore produces a spherical wavefront in an isovelocity medium.

The propagation loss caused by the spherical spreading can be written as $L_S(D) = 1/D$ [15]. Furthermore, when sound propagates in the ocean, part of the acoustic energy is continuously transformed into heat. This absorption is primarily a result of relaxation processes in seawater. The absorption loss can be written as [15]

$$L_A(D) = 10^{-D\beta/20000}, \quad (4)$$

where

$$\begin{aligned}\beta \;&=\; 8.68\cdot 10^3\left(\frac{Sl\cdot A\cdot f_T\cdot f_c^2}{f_T^2+f_c^2}+\frac{B\cdot f^2}{f_T}\right)\\ &\quad (1-6.54\cdot 10^{-4}\cdot P)\;\;[\mathrm{dB/km}], \end{aligned}\quad (5)$$

and $A = 2.34\cdot 10^{-6}$, $B = 3.38\cdot 10^{-6}$, Sl is salinity (in $\%\circ$), P is hydrostatic pressure [$\mathrm{kg/cm^2}$], f_c is the carrier frequency [kHz], $f_T = 21.9\cdot 10^{6-1520/(T+273)}$ is relaxation frequency [kHz], and T is the temperature [$^\circ C$].

The upward and downward arriving components of the input delay-spread function are, respectively,

$$h^{UA}_{pq}(t,\tau) = \sqrt{\frac{\eta_B}{2B(K+1)}} \quad (6)$$

$$\sum_{b=1}^{B}\sum_{\hat{s}=b-1}^{b} L_S(D^{UA}_{b\hat{s}})L_A(D^{UA}_{b\hat{s}})L_B(\theta^{UA}_{b\hat{s}})^b\sqrt{\frac{1}{M_{b\hat{s}}}}$$

$$\sum_{m=1}^{M_{b\hat{s}}}\sqrt{G_p\left(\alpha^{(p)}_{Tb\hat{s}m}\right)G_q\left(\alpha^{(q)}_{Rb\hat{s}m}\right)}\,\xi_{b\hat{s}m}e^{j\phi_{b\hat{s}m}}\delta\left(\tau-\tau^{(p,q)}_{b\hat{s}m}(t)\right),$$

$$h^{DA}_{pq}(t,\tau) = \sqrt{\frac{\eta_S}{2S(K+1)}} \quad (7)$$

$$\sum_{s=1}^{S}\sum_{\hat{b}=s-1}^{s} L_S(D^{DA}_{s\hat{b}})L_A(D^{DA}_{s\hat{b}})L_B(\theta^{DA}_{s\hat{b}})^{\hat{b}}\sqrt{\frac{1}{N_{s\hat{b}}}}$$

$$\sum_{n=1}^{N_{s\hat{b}}}\sqrt{G_p\left(\alpha^{(p)}_{Ts\hat{b}n}\right)G_q\left(\alpha^{(q)}_{Rs\hat{b}n}\right)}\,\xi_{s\hat{b}n}e^{j\phi_{s\hat{b}n}}\delta\left(\tau-\tau^{(p,q)}_{s\hat{b}n}(t)\right),$$

where $L_S(D^{UA}_{b\hat{s}})$ and $L_S(D^{DA}_{s\hat{b}})$ denote the macro-eigenray propagation losses caused by spherical spreading, $L_A(D^{UA}_{b\hat{s}})$ and $L_A(D^{DA}_{s\hat{b}})$ denote the macro-eigenray propagation losses caused by absorption, and $D^{UA}_{b\hat{s}}$ and $D^{DA}_{s\hat{b}}$ denote the total distances travelled by UA and DA macro-eigenrays with $\hat{s}, b$ and $s, \hat{b}$ surface-bottom interactions, respectively. The distances $D^{UA}_{b\hat{s}}$ and $D^{DA}_{s\hat{b}}$ are obtained using the method of images and can be written as [15]

$$D^{UA}_{b\hat{s}} \;=\; \sqrt{R^2+(2\hat{s}h-h_R+(-1)^{(b-\hat{s})}h_T)^2}, \quad (8)$$

$$D^{DA}_{s\hat{b}} \;=\; \sqrt{R^2+(2\hat{b}h+h_R-(-1)^{(s-\hat{b})}h_T)^2}. \quad (9)$$

TABLE I
DEFINITION OF THE PARAMETERS USED IN THE GEOMETRY-BASED MODEL FOR MIMO M-TO-M SWA CHANNELS.

R	The horizontal spacing between the Tx and Rx.
h, h_T, h_R	The water depth, the Tx depth, and the Rx depth, respectively.
d_T, d_R	The spacing between two adjacent transducer elements at the Tx and Rx, respectively.
θ_T, θ_R	The orientation of the Tx and Rx transducer array in the x-z plane (relative to the x-axis), respectively.
v_T, v_R	The velocities of the Tx and Rx, respectively.
γ_T, γ_R	The moving directions of the Tx and Rx, in the x-z plane (relative to the x-axis), respectively.
$\alpha^{(p)}_{Ts\hat{b}n}$, $\alpha^{(p)}_{Tb\hat{s}m}$	The angles of departure (AoD) of the waves that impinge on the scatterers $S^{(S)}_{s\hat{b}n}$ and $S^{(B)}_{b\hat{s}m}$, respectively.
$\alpha^{(q)}_{Rs\hat{b}n}$, $\alpha^{(q)}_{Rb\hat{s}m}$	The angles of arrival (AoA) of the waves scattered from $S^{(S)}_{s\hat{b}n}$ and $S^{(B)}_{b\hat{s}m}$, respectively.
α_{TR}, ε_{TR}	The AoA of line-of-sight path and the distance $O_T - O_R$, respectively.
$\epsilon^{(p)}_{Ts\hat{b}n}$, $\epsilon^{(p)}_{Tb\hat{s}m}$, $\epsilon^{(\tilde{p})}_{Ts\hat{b}n}$, $\epsilon^{(\tilde{p})}_{Tb\hat{s}m}$, $\epsilon^{(q)}_{Rs\hat{b}n}$, $\epsilon^{(q)}_{Rb\hat{s}m}$, $\epsilon^{(\tilde{q})}_{Rs\hat{b}n}$, $\epsilon^{(\tilde{q})}_{Rb\hat{s}m}$	The distances $d\left(T_x^{(p)}, S^{(S)}_{s\hat{b}n}\right)$, $d\left(T_x^{(p)}, S^{(B)}_{b\hat{s}m}\right)$, $d\left(T_x^{(\tilde{p})}, S^{(S)}_{s\hat{b}n}\right)$, $d\left(T_x^{(\tilde{p})}, S^{(B)}_{b\hat{s}m}\right)$, $d\left(S^{(S)}_{s\hat{b}n}, R_x^{(q)}\right)$, $d\left(S^{(B)}_{b\hat{s}m}, R_x^{(q)}\right)$, $d\left(S^{(S)}_{s\hat{b}n}, R_x^{(\tilde{q})}\right)$ and, $d\left(S^{(B)}_{b\hat{s}m}, R_x^{(\tilde{q})}\right)$, respectively.
ε_{pq}, $\varepsilon_{\tilde{p}q}$, $\varepsilon_{p\tilde{q}}$, $\varepsilon_{\tilde{p}\tilde{q}}$, $\varepsilon^{DA}_{Ts\hat{b}}$, $\varepsilon^{UA}_{Tb\hat{s}}$, $\varepsilon^{DA}_{Rs\hat{b}}$, $\varepsilon^{UA}_{Rb\hat{s}}$	The distances $d\left(T_x^{(p)}, R_x^{(q)}\right)$, $d\left(T_x^{(\tilde{p})}, R_x^{(q)}\right)$, $d\left(T_x^{(p)}, R_x^{(\tilde{q})}\right)$, $d\left(T_x^{(\tilde{p})}, R_x^{(\tilde{q})}\right)$, $d\left(O_T, S^{(S)}_{s\hat{b}}\right)$, $d\left(O_T, S^{(B)}_{b\hat{s}}\right)$, $d\left(S^{(S)}_{s\hat{b}}, O_R\right)$ and, $d\left(S^{(B)}_{b\hat{s}}, O_R\right)$, respectively.

The parameters η_S and η_B in (6) and (7), respectively, specify how much the UA and DA macro-eigenrays contribute in the total power, i.e., these parameters satisfy $\eta_S + \eta_B = 1$. The parameters $L_B(\theta^{DA}_{s\hat{b}})$ and $L_B(\theta^{UA}_{b\hat{s}})$ denote the impedance mismatch between the seawater and seabed and can be written as [15]

$$L_B(\theta) = \left| \frac{x\cos\theta - \sqrt{y^2 - \sin^2\theta}}{x\cos\theta + \sqrt{y^2 - \sin^2\theta}} \right|, \tag{10}$$

where $x = \rho_1/\rho$, $y = c/c_1$, ρ and c denote the density and sound speed in the seawater, respectively, whereas ρ_1 and c_1 denote the density and sound speed in the seabed, respectively. The incidence angles $\theta^{UA}_{b\hat{s}}$ and $\theta^{DA}_{s\hat{b}}$ are obtained as follows:

$$\theta^{UA}_{b\hat{s}} = \tan^{-1}\left(\frac{R}{2\hat{s}h - h_R + (-1)^{(b-\hat{s})}h_T}\right), \tag{11}$$

$$\theta^{DA}_{s\hat{b}} = \tan^{-1}\left(\frac{R}{2\hat{b}h + h_R - (-1)^{(s-\hat{b})}h_T}\right). \tag{12}$$

Finally, $\xi_{b\hat{s}m} > 0$ and $\xi_{s\hat{b}n} > 0$ denote the amplitudes of micro-eigenrays, $\phi_{b\hat{s}m}$ and $\phi_{s\hat{b}n}$ denote the phases of micro-eigenrays, and the time delays $\tau^{(p,q)}_{b\hat{s}m}(t)$ and $\tau^{(p,q)}_{s\hat{b}n}(t)$ are the travel times of UA and DA micro-eigenrays, respectively, i.e.,

$$\tau^{(p,q)}_{b\hat{s}m}(t) = \frac{D^{UA}_{b\hat{s}}}{c} - \frac{\epsilon^{UA}_{Tb\hat{s}} - \epsilon^{(p)}_{Tb\hat{s}m}}{c} - \frac{\epsilon^{UA}_{Rb\hat{s}} - \epsilon^{(q)}_{Rb\hat{s}m}}{c} + \frac{1}{c}\Delta Z_{b\hat{s}m}(t)\sin\alpha^{(q)}_{Rb\hat{s}m} + \frac{1}{c}\left[v_T t\cos(\alpha^{(p)}_{Tb\hat{s}m} - \gamma_T) + v_R t\cos(\alpha^{(q)}_{Rb\hat{s}m} - \gamma_R)\right], \tag{13}$$

$$\tau^{(p,q)}_{s\hat{b}n}(t) = \frac{D^{DA}_{s\hat{b}}}{c} - \frac{\epsilon^{DA}_{Ts\hat{b}} - \epsilon^{(p)}_{Ts\hat{b}n}}{c} - \frac{\epsilon^{DA}_{Rs\hat{b}} - \epsilon^{(q)}_{Rs\hat{b}n}}{c} + \frac{1}{c}\Delta Z_{s\hat{b}n}(t)\sin\alpha^{(q)}_{Rs\hat{b}n} + \frac{1}{c}\left[v_T t\cos(\alpha^{(p)}_{Ts\hat{b}n} - \gamma_T) + v_R t\cos(\alpha^{(q)}_{Rs\hat{b}n} - \gamma_R)\right], \tag{14}$$

where $\Delta Z_{s\hat{b}n}(t)$ and $\Delta Z_{b\hat{s}m}(t)$ denote the vertical displacements of surface micro-scatterers due to surface motion and the distances $\epsilon^{DA}_{Ts\hat{b}}$, $\epsilon^{DA}_{Rs\hat{b}}$, $\epsilon^{UA}_{Tb\hat{s}}$, and $\epsilon^{UA}_{Rb\hat{s}}$ are defined in Table I. The travel times of UA and DA micro-eigenrays take into account movement of the $\mathrm{T_x}$ and $\mathrm{R_x}$, the vertical displacements of surface micro-scatterers due to surface motion, and the location of MIMO hydrophones.

It is assumed that the AoDs ($\alpha^{(p)}_{Ts\hat{b}n}$ and $\alpha^{(p)}_{Tb\hat{s}m}$), the AoAs ($\alpha^{(q)}_{Rs\hat{b}n}$ and $\alpha^{(q)}_{Rb\hat{s}m}$), and the vertical displacements $\Delta Z_{s\hat{b}n}(t)$ and $\Delta Z_{b\hat{s}m}(t)$ are random variables. Furthermore, it is assumed that the phases $\phi_{s\hat{b}n}$ and $\phi_{b\hat{s}m}$ are uniform random variables on the interval $[-\pi, \pi)$ that are independent from the AoDs, the AoAs, and the vertical displacements of the surface. Here, we note that the locations of micro-scatterers that contribute to one macro-eigenray are independent from the locations of micro-scatterers that contribute to a different macro-eigenray because different macro-eigenrays have different angles of departure and arrival. Using the assumptions introduced above and the Central Limit Theorem [17], we can conclude that each macro-eigenray is an independent complex Gaussian process with zero mean. Sum of several complex Gaussian processes with zero means results in a new complex Gaussian process with zero mean. Hence, $h^{UA}_{pq}(t,\tau)$ and $h^{DA}_{pq}(t,\tau)$ are also independent complex Gaussian random processes with zero means. Note that the AoDs ($\alpha^{(p)}_{Ts\hat{b}n}$ and $\alpha^{(p)}_{Tb\hat{s}m}$) are dependent on the AoAs ($\alpha^{(q)}_{Rs\hat{b}n}$ and $\alpha^{(q)}_{Rb\hat{s}m}$), respectively. Assuming small angle spreads, $d_T \ll \min(h_T, h - h_T)$, and $d_R \ll \min(h_R, h - h_R)$, we can approximate the AoDs and AoAs in Fig. 3 as $\alpha^{(p)}_{Ts\hat{b}n} \approx \alpha^{(\tilde{p})}_{Ts\hat{b}n} \approx \alpha_{Ts\hat{b}n}$, $\alpha^{(p)}_{Tb\hat{s}m} \approx \alpha^{(\tilde{p})}_{Tb\hat{s}m} \approx \alpha_{Tb\hat{s}m}$, $\alpha^{(q)}_{Rs\hat{b}n} \approx \alpha^{(\tilde{q})}_{Rs\hat{b}n} \approx \alpha_{Rs\hat{b}n}$, and $\alpha^{(q)}_{Rb\hat{s}m} \approx \alpha^{(\tilde{q})}_{Rb\hat{s}m} \approx \alpha_{Rb\hat{s}m}$, where $\alpha_{Ts\hat{b}n}$, $\alpha_{Tb\hat{s}m}$, $\alpha_{Rs\hat{b}n}$, and $\alpha_{Rb\hat{s}m}$ are defined in Fig. 3. Assuming that each micro-eigenray, when interacting with the surface and bottom, has equal incident and reflecting angles, we can observe that $\alpha_{Ts\hat{b}n} = \pi - \alpha_{Rs\hat{b}n}$ and $\alpha_{Tb\hat{s}m} = 3\pi - \alpha_{Rb\hat{s}m}$.

The distances $\epsilon^{(p)}_{Ts\hat{b}n}$, $\epsilon^{(p)}_{Tb\hat{s}m}$, $\epsilon^{(q)}_{Rs\hat{b}n}$, $\epsilon^{(q)}_{Rb\hat{s}m}$, and ϵ_{pq} can be expressed as functions of the random AOAs $\alpha_{Rs\hat{b}n}$ and $\alpha_{Rb\hat{s}m}$ and the LoS angle α_{TR} as follows

$$\epsilon^{(p)}_{Ts\hat{b}n} \approx \frac{h_T}{\sin\alpha_{Rs\hat{b}n}} + \frac{L_t + 1 - 2p}{2} d_T\cos(\alpha_{Rs\hat{b}n} + \theta_T) \tag{15}$$

$$\epsilon^{(p)}_{Tb\hat{s}m} \approx -\frac{h - h_T}{\sin\alpha_{Rb\hat{s}m}} + \frac{L_t + 1 - 2p}{2} d_T\cos(\alpha_{Rb\hat{s}m} + \theta_T) \tag{16}$$

$$\epsilon^{(q)}_{Rs\hat{b}n} \approx \frac{h_R}{\sin\alpha_{Rs\hat{b}n}} - \frac{L_r + 1 - 2q}{2} d_R\cos(\alpha_{Rs\hat{b}n} - \theta_R) \tag{17}$$

$$\epsilon^{(q)}_{Rb\hat{s}m} \approx -\frac{h - h_R}{\sin\alpha_{Rb\hat{s}m}} - \frac{L_r + 1 - 2q}{2} d_R\cos(\alpha_{Rb\hat{s}m} - \theta_R) \tag{18}$$

$$\epsilon_{pq} \approx \epsilon_{TR} + \frac{L_t + 1 - 2p}{2} d_T\cos(\alpha_{TR} - \theta_T) - \frac{L_r + 1 - 2q}{2} d_R\cos(\alpha_{TR} - \theta_R) \tag{19}$$

where $\epsilon_{TR} = \sqrt{R^2 + (h_T - h_R)^2}$ and parameters p and q take values from the sets $p \in \{1, \ldots, L_t\}$ and $q \in \{1, \ldots, L_r\}$, respectively. The derivations of approximations in (15)-(19)

are presented in Appendix A. To simplify further analysis, we normalize all time delays with respect to the LoS arrival time. This normalization is reflected in the distances ϵ_{pq}, $D^{DA}_{s\hat{b}}$, and $D^{UA}_{b\hat{s}}$, and they can be rewritten as

$$\begin{aligned}\tilde{\epsilon}_{pq} &= 0.5(L_t+1-2p)d_T\cos(\alpha_{TR}-\theta_T)\\ &- 0.5(L_r+1-2q)d_R\cos(\alpha_{TR}-\theta_R), \quad (20)\\ \tilde{D}^{DA}_{s\hat{b}} &= \sqrt{R^2+(2\hat{b}h+h_R-(-1)^{(s-\hat{b})}h_T)^2}\\ &- \sqrt{R^2+(h_T-h_R)^2}, \quad (21)\\ \tilde{D}^{UA}_{b\hat{s}} &= \sqrt{R^2+(2\hat{s}h-h_R+(-1)^{(b-\hat{s})}h_T)^2}\\ &- \sqrt{R^2+(h_T-h_R)^2}. \quad (22)\end{aligned}$$

Since the depths h, h_T, and h_R are much smaller than the distance R, the distances $\tilde{D}^{DA}_{s\hat{b}}$ and $\tilde{D}^{UA}_{b\hat{s}}$ in (21) and (22) can be approximated using $\sqrt{1+x}\approx 1+x/2$, for small x, as follows

$$\begin{aligned}&\tilde{D}^{DA}_{s\hat{b}} \approx \quad (23)\\ &2\left[\hat{b}^2h^2+\hat{b}hh_R-(-1)^{(s-\hat{b})}\hat{b}hh_T+(s-\hat{b})h_Th_R\right]/R,\\ &\tilde{D}^{UA}_{b\hat{s}} \approx \quad (24)\\ &2\left[\hat{s}^2h^2-\hat{s}hh_R+(-1)^{(b-\hat{s})}\hat{s}hh_T+(b-\hat{s})h_Th_R\right]/R.\end{aligned}$$

Finally, we note that $\epsilon^{DA}_{Ts\hat{b}}$, $\epsilon^{DA}_{Rs\hat{b}}$, $\epsilon^{UA}_{Tb\hat{s}}$, and $\epsilon^{UA}_{Rb\hat{s}}$ can be written as functions of the mean AoA angles $\mu_{DAs\hat{b}}$ and $\mu_{UAb\hat{s}}$, i.e., $\epsilon^{DA}_{Ts\hat{b}}=h_T/\sin\mu_{DAs\hat{b}}$, $\epsilon^{DA}_{Rs\hat{b}}=h_R/\sin\mu_{DAs\hat{b}}$, $\epsilon^{UA}_{Tb\hat{s}}=-(h-h_T)/\sin\mu_{UAb\hat{s}}$, and $\epsilon^{UA}_{Rb\hat{s}}=-(h-h_R)/\sin\mu_{UAb\hat{s}}$, where the mean AoA angles $\mu_{DAs\hat{b}}$ and $\mu_{UAb\hat{s}}$ are depicted in Fig. 1.

The angles of arrival $\alpha_{Rs\hat{b}n}$ and $\alpha_{Rb\hat{s}m}$ are modeled using the following Gaussian probability density functions (pdfs)

$$\begin{aligned}&f_{\text{top}}(\alpha_{Rs\hat{b}n}) = \frac{1}{\sqrt{2\pi\sigma^2_{DAs\hat{b}}}}\\ &\exp\{-(\alpha_{Rs\hat{b}n}-\mu_{DAs\hat{b}})^2/(2\sigma^2_{DAs\hat{b}})\},\ 0<\alpha_{Rs\hat{b}n}<\pi, \quad (25)\\ &f_{\text{bottom}}(\alpha_{Rb\hat{s}m}) = \frac{1}{\sqrt{2\pi\sigma^2_{UAb\hat{s}}}}\\ &\exp\{-(\alpha_{Rb\hat{s}m}-\mu_{UAb\hat{s}})^2/(2\sigma^2_{UAb\hat{s}})\},\ \pi<\alpha_{Rb\hat{s}m}<2\pi, \quad (26)\end{aligned}$$

where $\mu_{DAs\hat{b}}$ and $\mu_{UAb\hat{s}}$ are the mean AoAs, whereas $\sigma_{DAs\hat{b}}$ and $\sigma_{UAb\hat{s}}$ are the angle spreads. The vertical displacements $\Delta Z_{s\hat{b}n}(t)$ and $\Delta Z_{b\hat{s}m}(t)$ are modeled as zero-mean Gaussian random processes with stationary and independent increments and can be written as

$$f(\Delta Z_{s\hat{b}n}(t)) = \frac{1}{\sqrt{2\pi t\zeta^2_{\Delta Z_{DAs\hat{b}}}}}e^{-(\Delta Z_{s\hat{b}n}(t))^2/(2t\zeta^2_{\Delta Z_{DAs\hat{b}}})} \quad (27)$$

$$f(\Delta Z_{b\hat{s}m}(t)) = \frac{1}{\sqrt{2\pi t\zeta^2_{\Delta Z_{UAb\hat{s}}}}}e^{-(\Delta Z_{b\hat{s}m}(t))^2/(2t\zeta^2_{\Delta Z_{UAb\hat{s}}})} \quad (28)$$

where $t\zeta^2_{\Delta Z_{DAs\hat{b}}}$ and $t\zeta^2_{\Delta Z_{UAb\hat{s}}}$ denote the variances.

To simplify further analysis, we use the time-variant transfer function instead of the input delay-spread function and we normalize the gain patterns of the transducer elements to unity (i.e., we assume omnidirectional array elements), although other gain patterns can be accommodated at this point. The time-variant transfer function is the Fourier transform of the input delay-spread function [17] and can be written as

$$\begin{aligned}T_{pq}(t,f) &= \mathcal{F}_\tau\{h_{pq}(t,\tau)\}\\ &= T^{LoS}_{pq}(t,f)+T^{UA}_{pq}(t,f)+T^{DA}_{pq}(t,f) \quad (29)\end{aligned}$$

where $T^{LoS}_{pq}(t,f)$, $T^{UA}_{pq}(t,f)$, and $T^{DA}_{pq}(t,f)$ are LoS, UA, and DA components of the time-variant transfer function, respectively. Using (2)-(24), the LoS, UA, and DA components of the time-variant transfer function in (29) can be written as

$$\begin{aligned}&T^{LoS}_{pq}(t,f)=\mathcal{F}_\tau\left\{h^{LoS}_{pq}(t,\tau)\right\}=\sqrt{\frac{K}{K+1}}L_S(\epsilon_{TR})L_A(\epsilon_{TR})\\ &e^{j\frac{2\pi}{c}(f_c+f)[v_Tt\cos(\alpha_{TR}-\gamma_T)-v_Rt\cos(\alpha_{TR}-\gamma_R)]} \quad (30)\\ &e^{j\frac{2\pi f_c}{c}[(0.5L_t+0.5-p)d_T\cos(\alpha_{TR}-\theta_T)-(0.5L_r+0.5-q)d_R\cos(\alpha_{TR}-\theta_R)]}\\ &T^{UA}_{pq}(t,f)=\mathcal{F}_\tau\left\{h^{UA}_{pq}(t,\tau)\right\}=\sqrt{\frac{\eta_B}{2B(K+1)}}\sum_{b=1}^{B}\sum_{\hat{s}=b-1}^{b}\\ &L_S(D^{UA}_{b\hat{s}})L_A(D^{UA}_{b\hat{s}})L_B(\theta^{UA}_{b\hat{s}})^b\sqrt{\frac{1}{M_{b\hat{s}}}}\sum_{m=1}^{M_{b\hat{s}}}\xi_{b\hat{s}m}e^{j\phi_{b\hat{s}m}} \quad (31)\\ &e^{-j\frac{2\pi(f_c+f)}{c}\left[\tilde{D}^{UA}_{b\hat{s}}-\frac{h_R+h_T-2h}{\sin\mu_{UAb\hat{s}}}+\frac{h_R+h_T-2h}{\sin\alpha_{Rb\hat{s}m}}\right]}\\ &e^{j\frac{2\pi(f_c+f)}{c}v_Tt\cos(\alpha_{Rb\hat{s}m}+\gamma_T)}\\ &e^{-j\frac{2\pi(f_c+f)}{c}[v_Rt\cos(\alpha_{Rb\hat{s}m}-\gamma_R)+\Delta Z_{b\hat{s}m}(t)\sin\alpha_{Rb\hat{s}m}]}\\ &e^{j\frac{2\pi f_c}{c}\left[\frac{L_t+1-2p}{2}d_T\cos(\alpha_{Rb\hat{s}m}+\theta_T)-\frac{L_r+1-2q}{2}d_R\cos(\alpha_{Rb\hat{s}m}-\theta_R)\right]}\\ &T^{DA}_{pq}(t,f)=\mathcal{F}_\tau\left\{h^{DA}_{pq}(t,\tau)\right\}=\sqrt{\frac{\eta_T}{2T(K+1)}}\sum_{s=1}^{S}\sum_{\hat{b}=s-1}^{s}\\ &L_S(D^{DA}_{s\hat{b}})L_A(D^{DA}_{s\hat{b}})L_B(\theta^{DA}_{s\hat{b}})^{\hat{b}}\sqrt{\frac{1}{N_{s\hat{b}}}}\sum_{n=1}^{N_{s\hat{b}}}\xi_{s\hat{b}n}e^{j\phi_{s\hat{b}n}} \quad (32)\\ &e^{-j\frac{2\pi(f_c+f)}{c}\left[\tilde{D}^{DA}_{s\hat{b}}-\frac{h_R+h_T}{\sin\mu_{DAs\hat{b}}}+\frac{h_R+h_T}{\sin\alpha_{Rs\hat{b}n}}\right]}\\ &e^{j\frac{2\pi(f_c+f)}{c}v_Tt\cos(\alpha_{Rs\hat{b}n}+\gamma_T)}\\ &e^{-j\frac{2\pi(f_c+f)}{c}\left[v_Rt\cos(\alpha_{Rs\hat{b}n}-\gamma_R)+\Delta Z_{s\hat{b}n}(t)\sin\alpha_{Rs\hat{b}n}\right]}\\ &e^{j\frac{2\pi f_c}{c}\left[\frac{L_t+1-2p}{2}d_T\cos(\alpha_{Rs\hat{b}n}+\theta_T)-\frac{L_r+1-2q}{2}d_R\cos(\alpha_{Rs\hat{b}n}-\theta_R)\right]},\end{aligned}$$

where f_c denotes the carrier frequency.

III. Time-Frequency Correlation Function, Doppler Power Spectral Density, and Delay Cross-Power Spectral Density of the MIMO M-to-M SWA Statistical Model

Assuming an isovelocity shallow water environment, we first derive the tf-cf of the MIMO geometry-based statistical model. From the tf-cf, we derive the corresponding D-psd and dc-psd and discuss some simulation results for the tf-cf, D-psd and dc-psd.

A. MIMO Time-Frequency Correlation Function

The normalized tf-cf between two time-variant transfer functions $T_{pq}(t_1,f_1)$ and $T_{\tilde{p}\tilde{q}}(t_2,f_2)$, is defined as [17]

$$R_{pq,\tilde{p}\tilde{q}}(t_1,f_1,t_2,f_2) = \frac{\mathrm{E}\left[T_{pq}(t_1,f_1)^*T_{\tilde{p}\tilde{q}}(t_2,f_2)\right]}{\sqrt{\mathrm{Var}[|T_{pq}(t_1,f_1)|^2]\mathrm{Var}[|T_{\tilde{p}\tilde{q}}(t_2,f_2)|^2]}}, \quad (33)$$

where $(\cdot)^*$ denotes complex conjugate operation, $\mathrm{E}[\cdot]$ is the statistical expectation operator, $\mathrm{Var}[\cdot]$ is the statistical variance operator, $p, \tilde{p} \in \{1, \ldots, L_t\}$, and $q, \tilde{q} \in \{1, \ldots, L_r\}$. Since $T_{pq}^{UA}(t, f)$ and $T_{pq}^{DA}(t, f)$ are independent zero-mean random processes, (33) can be simplified to

$$R_{pq,\tilde{p}\tilde{q}}(t_1, f_1, t_2, f_2) = R_{pq,\tilde{p}\tilde{q}}^{LoS}(t_1, f_1, t_2, f_2) + R_{pq,\tilde{p}\tilde{q}}^{UA}(t_1, f_1, t_2, f_2) + R_{pq,\tilde{p}\tilde{q}}^{DA}(t_1, f_1, t_2, f_2), \quad (34)$$

where $R_{pq,\tilde{p}\tilde{q}}^{LoS}(t_1, f_1, t_2, f_2)$, $R_{pq,\tilde{p}\tilde{q}}^{UA}(t_1, f_1, t_2, f_2)$, and $R_{pq,\tilde{p}\tilde{q}}^{DA}(t_1, f_1, t_2, f_2)$ denote the normalized tf-cfs of the LoS, UA, and DA components, respectively, and are defined as

$$R_{pq,\tilde{p}\tilde{q}}^{LoS}(t_1, f_1, t_2, f_2) = \frac{\mathrm{E}\left[T_{pq}^{LoS}(t_1, f_1)^* T_{\tilde{p}\tilde{q}}^{LoS}(t_2, f_2)\right]}{\Omega_{LoS}/(K+1)}, \quad (35)$$

$$R_{pq,\tilde{p}\tilde{q}}^{UA}(t_1, f_1, t_2, f_2) = \frac{\mathrm{E}\left[T_{pq}^{UA}(t_1, f_1)^* T_{\tilde{p}\tilde{q}}^{UA}(t_2, f_2)\right]}{\Omega_{UA}/(K+1)}, \quad (36)$$

$$R_{pq,\tilde{p}\tilde{q}}^{DA}(t_1, f_1, t_2, f_2) = \frac{\mathrm{E}\left[T_{pq}^{DA}(t_1, f_1)^* T_{\tilde{p}\tilde{q}}^{DA}(t_2, f_2)\right]}{\Omega_{DA}/(K+1)}, \quad (37)$$

where $\Omega_{LoS} = (L_S(\epsilon_{TR})L_A(\epsilon_{TR}))^2$, $\Omega_{UA} = \mathrm{E}[(L_S(D_{b\hat{s}}^{UA})$ $L_A(D_{b\hat{s}}^{UA})L_B(\theta_{b\hat{s}}^{UA})^{\hat{b}})^2]$, and $\Omega_{DA} = \mathrm{E}[(L_S(D_{s\hat{b}}^{DA})L_A(D_{s\hat{b}}^{DA})$ $L_B(\theta_{s\hat{b}}^{DA})^{\hat{b}})^2]$. Under the wide sense stationary uncorrelated scattering (WSSUS) condition, (34) simplifies to [17], [18]

$$R_{pq,\tilde{p}\tilde{q}}(\Delta t, \Delta f) = R_{pq,\tilde{p}\tilde{q}}^{LoS}(\Delta t, \Delta f) + R_{pq,\tilde{p}\tilde{q}}^{UA}(\Delta t, \Delta f) + R_{pq,\tilde{p}\tilde{q}}^{DA}(\Delta t, \Delta f), \quad (38)$$

where $\Delta t = t_2 - t_1$ and $\Delta f = f_2 - f_1$.

By substituting (30) into (35), the expression for the MIMO tf-cf of LoS component becomes

$$R_{pq,\tilde{p}\tilde{q}}^{LoS}(t_1, f_1, t_2, f_2) = K \quad (39)$$
$$e^{j\frac{2\pi f_c}{c}[v_T(t_2-t_1)\cos(\alpha_{TR}-\gamma_T)-v_R(t_2-t_1)\cos(\alpha_{TR}-\gamma_R)]}$$
$$e^{j\frac{2\pi f_1}{c}[v_T(t_2-t_1)\cos(\alpha_{TR}-\gamma_T)-v_R(t_2-t_1)\cos(\alpha_{TR}-\gamma_R)]}$$
$$e^{j\frac{2\pi(f_2-f_1)}{c}[v_T t_2\cos(\alpha_{TR}-\gamma_T)-v_R t_2\cos(\alpha_{TR}-\gamma_R)]}$$
$$e^{j\frac{2\pi f_c}{c}[(p-\tilde{p})d_T\cos(\alpha_{TR}-\theta_T)-(q-\tilde{q})d_R\cos(\alpha_{TR}-\theta_R)]}.$$

For WSSUS conditions, (39) simplifies to

$$R_{pq,\tilde{p}\tilde{q}}^{LoS}(\Delta t, \Delta f) = K$$
$$e^{j\frac{2\pi f_c}{c}[v_T\Delta t\cos(\alpha_{TR}-\gamma_T)-v_R\Delta t\cos(\alpha_{TR}-\gamma_R)]}$$
$$e^{j\frac{2\pi f_c}{c}[(p-\tilde{p})d_T\cos(\alpha_{TR}-\theta_T)-(q-\tilde{q})d_R\cos(\alpha_{TR}-\theta_R)]}. \quad (40)$$

As shown in Appendix B, the MIMO tf-cfs of the UA and DA components can be closely approximated as

$$R_{pq,\tilde{p}\tilde{q}}^{UA}(t_1, f_1, t_2, f_2) \approx \frac{\eta_B}{2B}\sum_{b=1}^{B}\sum_{\hat{s}=b-1}^{b} e^{-j\frac{2\pi(f_2-f_1)}{c}\tilde{D}_{b\hat{s}}^{UA}}$$
$$e^{j\frac{2\pi f_c}{c}[(p-\tilde{p})d_T\cos(\mu_{UAb\hat{s}}+\theta_T)-(q-\tilde{q})d_R\cos(\mu_{UAb\hat{s}}-\theta_R)]}$$
$$e^{j\frac{2\pi(f_c+f_1)}{c}[v_T(t_2-t_1)\cos(\mu_{UAb\hat{s}}+\gamma_T)-v_R(t_2-t_1)\cos(\mu_{UAb\hat{s}}-\gamma_R)]}$$
$$e^{j\frac{2\pi(f_2-f_1)}{c}[v_T t_2\cos(\mu_{UAb\hat{s}}+\gamma_T)-v_R t_2\cos(\mu_{UAb\hat{s}}-\gamma_R)]}$$
$$e^{-\frac{(t_2-t_1)\zeta_{\Delta Z_{UAb\hat{s}}}^2}{2}\left[\frac{2\pi(f_c+f_1)}{c}\sin\mu_{UAb\hat{s}}\right]^2}$$
$$e^{-\frac{t_2\zeta_{\Delta Z_{UAb\hat{s}}}^2}{2}\left[\frac{2\pi(f_2-f_1)}{c}\sin\mu_{UAb\hat{s}}\right]^2}\exp\left\{-\frac{\sigma_{UAb\hat{s}}^2}{2}\left[\frac{2\pi(f_2-f_1)}{c}\right.\right.$$
$$\frac{h_R+h_T-2h}{\sin\mu_{UAb\hat{s}}\tan\mu_{UAb\hat{s}}}+\frac{2\pi f_c}{c}(q-\tilde{q})d_R\sin(\mu_{UAb\hat{s}}-\theta_R)-$$
$$\frac{2\pi f_c}{c}(p-\tilde{p})d_T\sin(\mu_{UAb\hat{s}}+\theta_T)+$$
$$\frac{2\pi(f_2-f_1)}{c}[v_R t_2\sin(\mu_{UAb\hat{s}}-\gamma_R)-v_T t_2\sin(\mu_{UAb\hat{s}}+\gamma_T)]+$$
$$\frac{2\pi(f_c+f_1)}{c}[v_R(t_2-t_1)\sin(\mu_{UAb\hat{s}}-\gamma_R)-$$
$$v_T(t_2-t_1)\sin(\mu_{UAb\hat{s}}+\gamma_T)]+$$
$$(t_2-t_1)\zeta_{\Delta Z_{UAb\hat{s}}}^2\left[\frac{2\pi(f_c+f_1)}{c}\right]^2\sin\mu_{UAb\hat{s}}\cos\mu_{UAb\hat{s}}+$$
$$\left.\left.t_2\zeta_{\Delta Z_{UAb\hat{s}}}^2\left[\frac{2\pi(f_2-f_1)}{c}\right]^2\sin\mu_{UAb\hat{s}}\cos\mu_{UAb\hat{s}}\right]^2\right\}, \quad (41)$$

$$R_{pq,\tilde{p}\tilde{q}}^{DA}(t_1, f_1, t_2, f_2) \approx \frac{\eta_S}{2S}\sum_{s=1}^{S}\sum_{\hat{b}=s-1}^{s} e^{-j\frac{2\pi(f_2-f_1)}{c}\tilde{D}_{s\hat{b}}^{DA}}$$
$$e^{j\frac{2\pi f_c}{c}\left[(p-\tilde{p})d_T\cos(\mu_{DAs\hat{b}}+\theta_T)-(q-\tilde{q})d_R\cos(\mu_{DAs\hat{b}}-\theta_R)\right]}$$
$$e^{j\frac{2\pi(f_c+f_1)}{c}\left[v_T(t_2-t_1)\cos(\mu_{DAs\hat{b}}+\gamma_T)-v_R(t_2-t_1)\cos(\mu_{DAs\hat{b}}-\gamma_R)\right]}$$
$$e^{j\frac{2\pi(f_2-f_1)}{c}\left[v_T t_2\cos(\mu_{DAs\hat{b}}+\gamma_T)-v_R t_2\cos(\mu_{DAs\hat{b}}-\gamma_R)\right]}$$
$$e^{-\frac{(t_2-t_1)\zeta_{\Delta Z_{DAs\hat{b}}}^2}{2}\left[\frac{2\pi(f_c+f_1)}{c}\sin\mu_{DAs\hat{b}}\right]^2}$$
$$e^{-\frac{t_2\zeta_{\Delta Z_{DAs\hat{b}}}^2}{2}\left[\frac{2\pi(f_2-f_1)}{c}\sin\mu_{DAs\hat{b}}\right]^2}\exp\left\{-\frac{\sigma_{DAs\hat{b}}^2}{2}\left[\frac{2\pi(f_2-f_1)}{c}\right.\right.$$
$$\frac{h_R+h_T}{\sin\mu_{DAs\hat{b}}\tan\mu_{DAs\hat{b}}}+\frac{2\pi f_c}{c}(q-\tilde{q})d_R\sin(\mu_{DAs\hat{b}}-\theta_R)-$$
$$\frac{2\pi f_c}{c}(p-\tilde{p})d_T\sin(\mu_{DAs\hat{b}}+\theta_T)+\frac{2\pi(f_c+f_1)}{c}$$
$$\left[v_R(t_2-t_1)\sin(\mu_{DAs\hat{b}}-\gamma_R)-v_T(t_2-t_1)\sin(\mu_{DAs\hat{b}}+\gamma_T)\right]+$$
$$\frac{2\pi(f_2-f_1)}{c}\left[v_R t_2\sin(\mu_{DAs\hat{b}}-\gamma_R)-v_T t_2\sin(\mu_{DAs\hat{b}}+\gamma_T)\right]+$$
$$(t_2-t_1)\zeta_{\Delta Z_{DAs\hat{b}}}^2\left[\frac{2\pi(f_c+f_1)}{c}\right]^2\sin\mu_{DAs\hat{b}}\cos\mu_{DAs\hat{b}}+$$
$$\left.\left.t_2\zeta_{\Delta Z_{DAs\hat{b}}}^2\left[\frac{2\pi(f_2-f_1)}{c}\right]^2\sin\mu_{DAs\hat{b}}\cos\mu_{DAs\hat{b}}\right]^2\right\}. \quad (42)$$

Under WSSUS conditions, (41) and (42) simplify to

$$R_{pq,\tilde{p}\tilde{q}}^{UA}(\Delta t, \Delta f) = \frac{\eta_B}{2B}\sum_{b=1}^{B}\sum_{\hat{s}=b-1}^{b} e^{-\frac{\Delta t\zeta_{\Delta Z_{UAb\hat{s}}}^2}{2}\left[\frac{2\pi}{\lambda}\sin\mu_{UAb\hat{s}}\right]^2}$$
$$e^{j\frac{2\pi}{\lambda}(p-\tilde{p})d_T\cos(\mu_{UAb\hat{s}}+\theta_T)-j\frac{2\pi\Delta f}{c}\tilde{D}_{b\hat{s}}^{UA}-j\frac{2\pi}{\lambda}v_R\Delta t\cos(\mu_{UAb\hat{s}}-\gamma_R)}$$
$$e^{j\frac{2\pi}{\lambda}[-(q-\tilde{q})d_R\cos(\mu_{UAb\hat{s}}-\theta_R)+v_T\Delta t\cos(\mu_{UAb\hat{s}}+\gamma_T)]}$$
$$\exp\left\{-\frac{\sigma_{UAb\hat{s}}^2}{2}\left[\frac{2\pi\Delta f}{c}\frac{h_R+h_T-2h}{\sin\mu_{UAb\hat{s}}\tan\mu_{UAb\hat{s}}}+\right.\right.$$
$$\frac{2\pi}{\lambda}[(q-\tilde{q})d_R\sin(\mu_{UAb\hat{s}}-\theta_R)-(p-\tilde{p})d_T\sin(\mu_{UAb\hat{s}}+\theta_T)]+$$
$$\frac{2\pi}{\lambda}[v_R\Delta t\sin(\mu_{UAb\hat{s}}-\gamma_R)-v_T\Delta t\sin(\mu_{UAb\hat{s}}+\gamma_T)]+$$
$$\left.\left.\Delta t\zeta_{\Delta Z_{UAb\hat{s}}}^2\left[\frac{2\pi}{\lambda}\right]^2\sin\mu_{UAb\hat{s}}\cos\mu_{UAb\hat{s}}\right]^2\right\}, \quad (43)$$

$$R_{pq,\tilde{p}\tilde{q}}^{DA}(\Delta t, \Delta f) = \frac{\eta_S}{2S}\sum_{s=1}^{S}\sum_{\hat{b}=s-1}^{s} e^{-\frac{\Delta t\zeta_{\Delta Z_{DAs\hat{b}}}^2}{2}\left[\frac{2\pi}{\lambda}\sin\mu_{DAs\hat{b}}\right]^2}$$
$$e^{j\frac{2\pi}{\lambda}(q-\tilde{q})d_R\cos(\mu_{DAs\hat{b}}-\theta_R)-j\frac{2\pi\Delta f}{c}\tilde{D}_{s\hat{b}}^{DA}-v_R\Delta t\cos(\mu_{DAs\hat{b}}-\gamma_R)}$$
$$e^{j\frac{2\pi}{\lambda}\left[-(p-\tilde{p})d_T\cos(\mu_{DAs\hat{b}}+\theta_T)+v_T\Delta t\cos(\mu_{DAs\hat{b}}+\gamma_T)\right]}$$

$$\exp\Bigg\{-\frac{\sigma^2_{DAs\hat{b}}}{2}\Bigg[\frac{2\pi\Delta f}{c}\frac{h_R+h_T}{\sin\mu_{DAs\hat{b}}\tan\mu_{DAs\hat{b}}}+\frac{2\pi}{\lambda}$$
$$\big[(q-\tilde{q})d_R\sin(\mu_{DAs\hat{b}}-\theta_R)-(p-\tilde{p})d_T\sin(\mu_{DAs\hat{b}}+\theta_T)\big]+$$
$$\frac{2\pi}{\lambda}\left[v_R\Delta t\sin(\mu_{DAs\hat{b}}-\gamma_R)-v_T\Delta t\sin(\mu_{DAs\hat{b}}+\gamma_T)\right]+$$
$$\Delta t\zeta^2_{\Delta Z_{DAs\hat{b}}}\left[\frac{2\pi f_c}{c}\right]^2\sin\mu_{DAs\hat{b}}\cos\mu_{DAs\hat{b}}\Bigg]^2\Bigg\}, \quad (44)$$

where λ denotes the carrier wavelength.

From (39), (41), and (42) we can observe that the tf-cf of SWA channel follows an exponential function. This result is in agreement with the experimentally obtained tf-cfs [6], [13], [14]. Furthermore, this result differs from the traditional Bessel-shaped tf-cfs that are typical for radio channels. These differences are due to different propagation mechanisms in SWA and radio channels. Fig. 4 plots several single-input single-output (SISO) and MIMO tf-cfs as function of time, assuming WSSUS isovelocity scattering environment. We as-

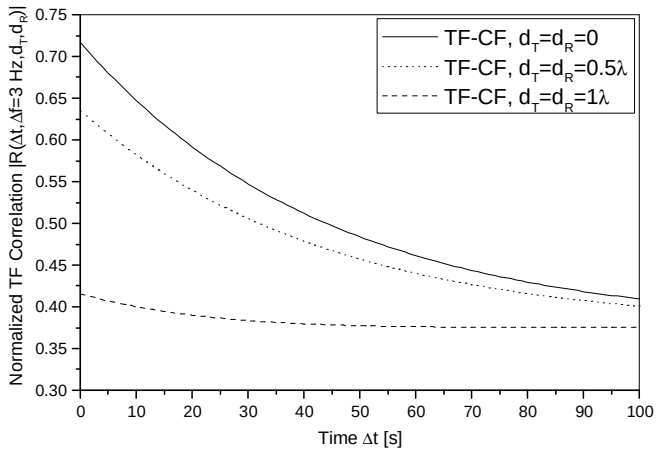

Fig. 4. The magnitude of MIMO time-frequency correlation function as a function of time, for $\Delta f = 3$ Hz and $d_T = d_R = [0, 0.5\lambda, 1\lambda]$.

sume that the carrier frequency is $f_c = 1.7$ kHz and the speed of sound is $c = 1500$ m/s. The distance between the $\mathrm{T_x}$ and $\mathrm{R_x}$ is set to $R = 2$ km, while the water, $\mathrm{T_x}$, and $\mathrm{R_x}$ depths are $h = 100$ m, $h_T = 50$ m, and $h_R = 50$ m, respectively. The $\mathrm{T_x}$ and $\mathrm{R_x}$ have $L_t = L_r = 2$ vertically oriented elements (i.e., $\theta_T = \theta_R = 90°$). It is assumed that the $\mathrm{T_x}$ and $\mathrm{R_x}$ are stationary, i.e., $v_T = v_R = 0$ m/s. The spacing between the $\mathrm{T_x}$ and $\mathrm{R_x}$ transducer elements are chosen from the set $d_T = d_R \in [0, 0.5\lambda, 1\lambda]$. For illustration purposes, the rest of the model parameters are chosen to be: $K = 0.6$, $S = B = 1$, $\zeta_{\Delta Z_{DA10}} = \zeta_{\Delta Z_{DA11}} = \zeta_{\Delta Z_{UA10}} = \zeta_{\Delta Z_{UA11}} = 0.1$, $\eta_S = 0.6$, $\mu_{DA10} = 166°$, $\mu_{DA11} = 163.5°$, $\mu_{UA10} = 191.9°$, $\mu_{UA11} = 192.9°$, $\sigma_{DA10} = 2.5°$, $\sigma_{DA11} = 4°$, $\sigma_{UA10} = 2.4°$, $\sigma_{UA11} = 3°$, $\alpha_{TR} = 180°$. The frequency deviation in Fig. 4 is set to $\Delta f = 3$ Hz. The parameters used to obtain the curves in Fig. 4 are summarized in the forth column of Table II. We can observe that the tf-cf decreases as the spacings between the $\mathrm{T_x}$ and $\mathrm{R_x}$ elements, i.e., d_T and d_R, increase.

B. MIMO Doppler Power Spectral Density

The D-psd of the time-variant transfer function is the Fourier transform of the time-frequency correlation function $R_{pq,\tilde{p}\tilde{q}}(\Delta t, \Delta f = 0)$ with respect to Δt [17], [18]. From (34), it follows that the D-psd is a summation of the D-psd functions of the LoS, UA, and DA components, i.e.,

$$S_{pq,\tilde{p}\tilde{q}}(\nu) = S^{LoS}_{pq,\tilde{p}\tilde{q}}(\nu) + S^{UA}_{pq,\tilde{p}\tilde{q}}(\nu) + S^{DA}_{pq,\tilde{p}\tilde{q}}(\nu). \quad (45)$$

By calculating the Fourier transform of the tf-cf in (40), we obtain the MIMO D-psd of the LoS component as follows

$$S^{LoS}_{pq,\tilde{p}\tilde{q}}(\nu) = \mathcal{F}_{\Delta t}\{R^{LoS}_{pq,\tilde{p}\tilde{q}}(\Delta t, \Delta f = 0)\} =$$
$$Ke^{j\frac{2\pi}{\lambda}[(p-\tilde{p})d_T\cos(\alpha_{TR}-\theta_T)-(q-\tilde{q})d_R\cos(\alpha_{TR}-\theta_R)]}$$
$$\delta\Big(\nu-\frac{v_R}{\lambda}\cos(\alpha_{TR}-\gamma_R)+\frac{v_T}{\lambda}\cos(\alpha_{TR}-\gamma_T)\Big). \quad (46)$$

As shown in Appendix C, the D-psds of the UA and DA components are, respectively,

$$S^{UA}_{pq,\tilde{p}\tilde{q}}(\nu) = \frac{\eta_B}{2B}\sum_{b=1}^{B}\sum_{\hat{s}=b-1}^{b}e^{-\frac{\sigma^2_{UAb\hat{s}}}{2}B^2_{UAb\hat{s}}}$$
$$e^{\frac{\left(j2\pi\nu+C_{UAb\hat{s}}+0.5\sigma^2_{UAb\hat{s}}A_{UAb\hat{s}}B_{UAb\hat{s}}\right)^2}{\sigma^4_{UAb\hat{s}}A^2_{UAb\hat{s}}}}\frac{\sqrt{\pi}}{0.5\sigma^2_{UAb\hat{s}}A_{UAb\hat{s}}}$$
$$e^{j\frac{2\pi}{\lambda}[(p-\tilde{p})d_T\cos(\mu_{UAb\hat{s}}+\theta_T)-(q-\tilde{q})d_R\cos(\mu_{UAb\hat{s}}-\theta_R)]}, \quad (47)$$

$$S^{DA}_{pq,\tilde{p}\tilde{q}}(\nu) = \frac{\eta_S}{2S}\sum_{s=1}^{S}\sum_{\hat{b}=s-1}^{s}e^{-\frac{\sigma^2_{DAs\hat{b}}}{2}B^2_{DAs\hat{b}}}$$
$$e^{\frac{\left(j2\pi\nu+C_{DAs\hat{b}}+0.5\sigma^2_{DAs\hat{b}}A_{DAs\hat{b}}B_{DAs\hat{b}}\right)^2}{\sigma^4_{DAs\hat{b}}A^2_{DAs\hat{b}}}}\frac{\sqrt{\pi}}{0.5\sigma^2_{DAs\hat{b}}A_{DAs\hat{b}}}$$
$$e^{j\frac{2\pi}{\lambda}\left[(p-\tilde{p})d_T\cos(\mu_{DAs\hat{b}}+\theta_T)-(q-\tilde{q})d_R\cos(\mu_{DAs\hat{b}}-\theta_R)\right]}, \quad (48)$$

where $A_{UAb\hat{s}}$, $B_{UAb\hat{s}}$, $C_{UAb\hat{s}}$, $A_{DAs\hat{b}}$, $B_{DAs\hat{b}}$, and $C_{DAs\hat{b}}$ are

$$A_{UAb\hat{s}} = \zeta^2_{\Delta Z_{UAb\hat{s}}}\left[\frac{2\pi}{\lambda}\right]^2\sin\mu_{UAb\hat{s}}\cos\mu_{UAb\hat{s}}+$$
$$\frac{2\pi}{\lambda}[v_R\sin(\mu_{UAb\hat{s}}-\gamma_R)-v_T\sin(\mu_{UAb\hat{s}}+\gamma_T)] \quad (49)$$

$$B_{UAb\hat{s}} = -\frac{2\pi}{\lambda}(p-\tilde{p})d_T\sin(\mu_{UAb\hat{s}}+\theta_T)+$$
$$\frac{2\pi}{\lambda}(q-\tilde{q})d_R\sin(\mu_{UAb\hat{s}}-\theta_R), \quad (50)$$

$$C_{UAb\hat{s}} = \frac{\zeta^2_{\Delta Z_{UAb\hat{s}}}}{2}\left[\frac{2\pi}{\lambda}\sin\mu_{UAb\hat{s}}\right]^2+$$
$$j\frac{2\pi}{\lambda}\left[v_R\cos(\mu_{UAb\hat{s}}-\gamma_R)-v_T\cos(\mu_{UAb\hat{s}}+\gamma_T)\right], \quad (51)$$

$$A_{DAs\hat{b}} = \zeta^2_{\Delta Z_{DAs\hat{b}}}\left[\frac{2\pi}{\lambda}\right]^2\sin\mu_{DAs\hat{b}}\cos\mu_{DAs\hat{b}}+$$
$$\frac{2\pi}{\lambda}\left[v_R\sin(\mu_{DAs\hat{b}}-\gamma_R)-v_T\sin(\mu_{DAs\hat{b}}+\gamma_T)\right] \quad (52)$$

$$B_{DAs\hat{b}} = -\frac{2\pi}{\lambda}(p-\tilde{p})d_T\sin(\mu_{DAs\hat{b}}+\theta_T)+$$
$$\frac{2\pi}{\lambda}(q-\tilde{q})d_R\sin(\mu_{DAs\hat{b}}-\theta_R), \quad (53)$$

$$C_{DAs\hat{b}} = \frac{\zeta^2_{\Delta Z_{DAs\hat{b}}}}{2}\left[\frac{2\pi}{\lambda}\sin\mu_{DAs\hat{b}}\right]^2+$$
$$j\frac{2\pi}{\lambda}\left[v_R\cos(\mu_{DAs\hat{b}}-\gamma_R)-v_T\cos(\mu_{DAs\hat{b}}+\gamma_T)\right]. \quad (54)$$

Fig. 5 shows several SISO and MIMO D-psds. We assume WSSUS isovelocity scattering environment with the carrier

frequency $f_c = 10$ kHz, and the speed of sound $c = 1500$ m/s. Furthermore, we choose the distance between the $\mathrm{T_x}$ and $\mathrm{R_x}$ to be $R = 2$ km. The water, $\mathrm{T_x}$, and $\mathrm{R_x}$ depths are chosen to be $h = 50$ m, $h_T = 18$ m, and $h_R = 18$ m, respectively. The $\mathrm{T_x}$ and $\mathrm{R_x}$ have $L_t = L_r = 2$ transducer elements with orientations $\theta_T = \theta_R = 90°$. The $\mathrm{T_x}$ and $\mathrm{R_x}$ are moving with speeds $v_T = v_R = 2$ m/s and have orientations $\gamma_T = \gamma_R = 40°$. The spacing between the $\mathrm{T_x}$ and $\mathrm{R_x}$ transducer elements are chosen from the set $d_T = d_R \in [0, 0.5\lambda, 1\lambda]$. The rest of the model parameters are chosen to be: $K = 0.6$, $S = B = 1$, $\zeta_{\Delta Z_{DA10}} = \zeta_{\Delta Z_{DA11}} = \zeta_{\Delta Z_{UA10}} = \zeta_{\Delta Z_{UA11}} = 0.09$, $\mu_{DA10} = 178°$, $\mu_{DA11} = 177°$, $\mu_{UA10} = 182°$, $\mu_{UA11} = 183°$, $\sigma_{DA10} = 10°$, $\sigma_{DA11} = 13.6°$, $\sigma_{UA10} = 10°$, $\sigma_{UA11} = 13.6°$, $\alpha_{TR} = 180°$, $\eta_S = 0.4$, and $\eta_B = 1 - \eta_S$. The parameters used to obtain the curves in Fig. 5 are summarized in the fifth column of Table II. From Fig. 5, we can observe that the D-psd magnitude and the Doppler spread decrease as the spacings between the $\mathrm{T_x}$ and $\mathrm{R_x}$ elements increase. On the other hand, the Doppler shift remains unchanged. Finally, we note that the D-psd of SWA channels differs from the U-shaped D-psd in cellular radio channels due to different propagation mechanisms.

C. MIMO Delay Cross-Power Spectral Density

The dc-psd of the time-variant transfer function is the inverse Fourier transform of the time-frequency correlation function $R_{pq,\tilde{p}\tilde{q}}(\Delta t = 0, \Delta f)$ with respect to Δf [17], [18]. From (34), it follows that the dc-psd is a summation of the dc-psd functions of the LoS, UA, and DA components, i.e.,

$$P_{pq,\tilde{p}\tilde{q}}(\tau) = P^{LoS}_{pq,\tilde{p}\tilde{q}}(\tau) + P^{UA}_{pq,\tilde{p}\tilde{q}}(\tau) + P^{DA}_{pq,\tilde{p}\tilde{q}}(\tau). \quad (55)$$

By calculating the inverse Fourier transform of the tf-cf in (40), we obtain the dc-psd of the LoS component as follows

$$P^{LoS}_{pq,\tilde{p}\tilde{q}}(\tau) = \mathcal{F}^{-1}_{\Delta f}\{R^{LoS}_{pq,\tilde{p}\tilde{q}}(\Delta t = 0, \Delta f)\} = K e^{j\frac{2\pi}{\lambda}[(p-\tilde{p})d_T \cos(\alpha_{TR}-\theta_T)-(q-\tilde{q})d_R\cos(\alpha_{TR}-\theta_R)]}\delta(\tau). \quad (56)$$

It can be shown that the dc-psd of the UA and DA components are, respectively,

$$P^{UA}_{pq,\tilde{p}\tilde{q}}(\tau) = \frac{\eta_B}{2B}\sum_{b=1}^{B}\sum_{\hat{s}=b-1}^{b} e^{-\frac{\sigma^2_{UAb\hat{s}}}{2}B^2_{UAb\hat{s}}} \quad (57)$$
$$e^{j\frac{2\pi}{\lambda}[(p-\tilde{p})d_T\cos(\mu_{UAb\hat{s}}+\theta_T)-(q-\tilde{q})d_R\cos(\mu_{UAb\hat{s}}-\theta_R)]}$$
$$e^{\frac{\left(j2\pi\tau - j2\pi\tilde{D}^{UA}_{b\hat{s}}/c - 0.5\sigma^2_{UAb\hat{s}}E_{UAb\hat{s}}B_{UAb\hat{s}}\right)^2}{\sigma^4_{UAb\hat{s}}E^2_{UAb\hat{s}}}}\frac{\sqrt{\pi}}{0.5\sigma^2_{UAb\hat{s}}E_{UAb\hat{s}}},$$

$$P^{DA}_{pq,\tilde{p}\tilde{q}}(\tau) = \frac{\eta_S}{2S}\sum_{s=1}^{S}\sum_{\hat{b}=s-1}^{s} e^{-\frac{\sigma^2_{DAs\hat{b}}}{2}B^2_{DAs\hat{b}}} \quad (58)$$
$$e^{j\frac{2\pi}{\lambda}\left[(p-\tilde{p})d_T\cos(\mu_{DAs\hat{b}}+\theta_T)-(q-\tilde{q})d_R\cos(\mu_{DAs\hat{b}}-\theta_R)\right]}$$
$$e^{\frac{\left(j2\pi\tau - j2\pi\tilde{D}^{DA}_{s\hat{b}}/c - 0.5\sigma^2_{DAs\hat{b}}E_{DAs\hat{b}}B_{DAs\hat{b}}\right)^2}{\sigma^4_{DAs\hat{b}}E^2_{DAs\hat{b}}}}\frac{\sqrt{\pi}}{0.5\sigma^2_{DAs\hat{b}}E_{DAs\hat{b}}},$$

where $B_{UAb\hat{s}}$ and $B_{DAs\hat{b}}$ are defined in (50) and (53), respectively, while $E_{UAb\hat{s}}$ and $E_{DAs\hat{b}}$ are defined as

$$E_{UAb\hat{s}} = \frac{2\pi}{c}\frac{h_R + h_T - 2h}{\sin\mu_{UAb\hat{s}}\tan\mu_{UAb\hat{s}}}, \quad (59)$$

$$E_{DAs\hat{b}} = \frac{2\pi}{c}\frac{h_R + h_T}{\sin\mu_{DAs\hat{b}}\tan\mu_{DAs\hat{b}}}. \quad (60)$$

The derivations of (57) and (58) are omitted for brevity.

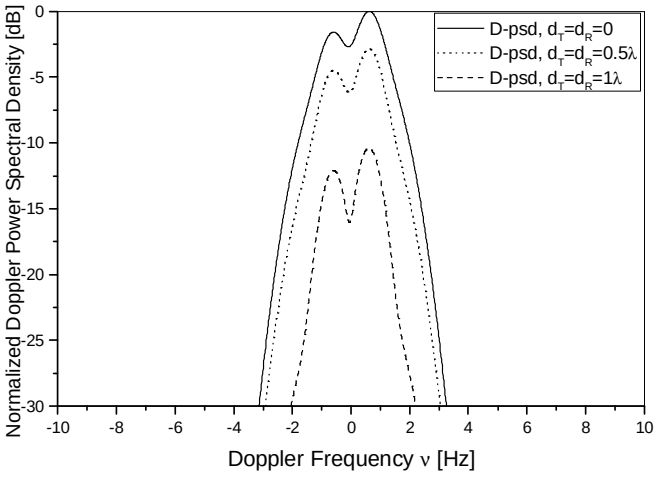

Fig. 5. The normalized MIMO Doppler power spectral density for $d_T = d_R = [0, 0.5\lambda, 1\lambda]$.

Fig. 6 plots several SISO and MIMO dc-psds, assuming WSSUS isovelocity scattering environment. We assume that the carrier frequency is $f_c = 17$ kHz and the speed of sound is $c = 1500$ m/s. The distance between the $\mathrm{T_x}$ and $\mathrm{R_x}$ is set to $R = 2$ km, while the water, $\mathrm{T_x}$, and $\mathrm{R_x}$ depths are $h = 50$ m, $h_T = 18$ m, and $h_R = 18$ m, respectively. The $\mathrm{T_x}$ and $\mathrm{R_x}$ have $L_t = L_r = 2$ vertically oriented elements (i.e., $\theta_T = \theta_R = 90°$). It is assumed that the $\mathrm{T_x}$ and $\mathrm{R_x}$ are stationary, i.e., $v_T = v_R = 0$ m/s. The spacing between the $\mathrm{T_x}$ and $\mathrm{R_x}$ transducer elements are chosen from the set $d_T = d_R \in [0, 1\lambda, 2\lambda]$. The rest of the model parameters are set to: $K = 0$, $S = B = 1$, $\zeta_{\Delta Z_{DA10}} = \zeta_{\Delta Z_{DA11}} = \zeta_{\Delta Z_{UA10}} = \zeta_{\Delta Z_{UA11}} = 0.1$, $\mu_{DA10} = 160°$, $\mu_{DA11} = 157°$, $\mu_{UA10} = 190°$, $\mu_{UA11} = 191°$, $\sigma_{DA10} = 2.55°$, $\sigma_{DA11} = 3.1°$, $\sigma_{UA10} = 4°$, $\sigma_{UA11} = 6°$, $\alpha_{TR} = 180°$, $\eta_S = 0.8$, and $\eta_B = 1 - \eta_S$. The parameters used to obtain the curves in Fig. 6 are summarized in the sixth column of Table II. From Fig. 6, we can observe that the magnitude of dc-psd and the multipath spread decrease as the spacing between the $\mathrm{T_x}$ and $\mathrm{R_x}$ elements increase. In contrast to radio channels, where the later arriving multipaths carry less energy than the earlier arriving multipaths (i.e., the dc-psd decays exponentially), in SWA channels, it is often the case that the later arriving multipaths are received as stronger signals that the earlier arriving multipaths. This phenomenon can be explained by observing how macro-eigenrays propagate through the waveguide. Note that macro-eigenrays cannot be received with equal strength at all vertical locations in water because their angles of departure and arrival are predetermined by the waveguide geometry. For example, if the hydrophone is placed near the center of waveguide (water column), most of the arriving macro-eigenrays can be detected and the dc-psd decays exponentially ($d_T = d_R = 0$ in Fig. 6). As the hydrophones move away from the center of waveguide, some macro-eigenrays, although arriving, cannot be recorded at new vertical location, causing the imbalance in the dc-psd function ($d_T = d_R = 2\lambda$ in Fig. 6).

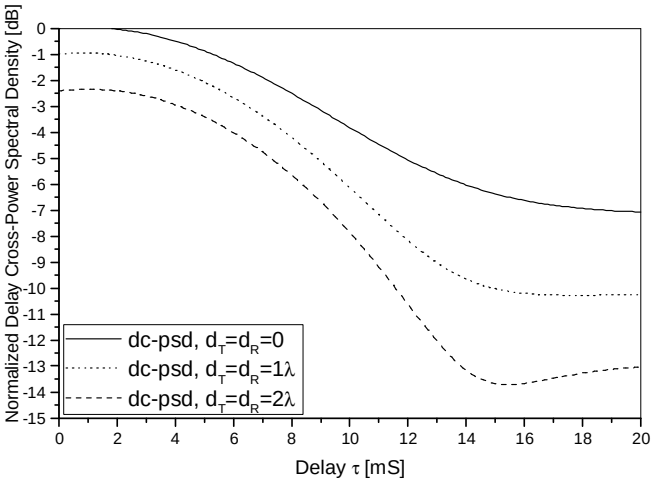

Fig. 6. The normalized MIMO delay cross-power spectral density for $d_T = d_R = [0, 1\lambda, 2\lambda]$.

IV. Comparison with Measured Data

In this section, we compare the theoretical results in Section III with the AUVFest07 measured data in [13], collected at calm sea. Furthermore, we compare the derived spatial correlation function $R_{pq,\tilde{p}\tilde{q}}(\Delta t = 0, \Delta f = 0)$ in (38) with the spatial correlation functions of the exponential model in [14], the particle-velocity model in [12], and the ASCOT01 measured data in [14].

The channel measurements in [13] are collected at $f_c = 17$ kHz and the speed of sound is $c = 1470$ m/s. The distance between the $\mathrm{T_x}$ and $\mathrm{R_x}$ is $R = 5$ km. The water, $\mathrm{T_x}$, and $\mathrm{R_x}$ depths are $h = 20$ m, $h_T = 19$ m, and $h_R = 18$ m, respectively. The $\mathrm{T_x}$ and $\mathrm{R_x}$ are equipped with vertically oriented transducer elements (i.e., $\theta_T = \theta_R = 90°$). It is assumed that the $\mathrm{T_x}$ and $\mathrm{R_x}$ are relatively stationary, i.e., slightly moving with waves (i.e., $\gamma_T = \gamma_R = 90°$).

Figs. 7 and 8 compare the analytical temporal and frequency correlation functions, i.e., $R_{11,11}(\Delta t, 0)$ and $R_{11,11}(0, \Delta f)$ in (38), with the measured temporal and frequency correlation functions, respectively. Furthermore, Figs. 9 and 10 compare the analytical and measured D-psds and dc-psds, respectively. The analytical curves in Figs. 7 - 10 are obtained with the parameters $K = 0.8$, $S = B = 1$, $v_T = 0.0006$ m/s, $v_R = 0.00025$ m/s, $\mu_{DA10} = 169°$, $\mu_{DA11} = 167°$, $\mu_{UA10} = 194°$, $\mu_{UA11} = 195°$, $\sigma_{DA10} = 3.25°$, $\sigma_{DA11} = 5°$, $\sigma_{UA10} = 2.7°$, $\sigma_{UA11} = 3.2°$, $\zeta_{\Delta Z_{DA10}} = \zeta_{\Delta Z_{DA11}} = 0.0097$, $\zeta_{\Delta Z_{UA10}} = \zeta_{\Delta Z_{UA11}} = 0.0087$, $\eta_S = 0.28$, and $\eta_B = 1 - \eta_S$. The Rice factor K is estimated using the moment-method in [20], and the parameters S and B are visually estimated from Fig. 3c in [13]. The rest of the parameters, i.e., $[v_T, v_R, \zeta_{\Delta Z_{DAs\hat{b}}}, \zeta_{\Delta Z_{UAb\hat{s}}}, \mu_{DAs\hat{b}}, \mu_{UAb\hat{s}}, \sigma_{DAs\hat{b}}, \sigma_{UAb\hat{s}}, \eta_S]$ are estimated jointly using the maximum-likelihood approach in [21] and the constraint $\eta_S + \eta_B = 1$. The maximum-likelihood function is optimized using the sequential quadratic programming algorithm [22], which is implemented in Matlab as a "fminsearch" function. The parameters used to obtain the curves in Figs. 7- 10 are summarized in the seventh column of Table II.

TABLE II
PARAMETERS USED IN FIGS. 4 - 11.

Parameters	Definition	Type	Figs 4	Fig. 5	Fig.6	Fig.7-Fig. 10	Fig.11
R [km]	The distance between the Tx and Rx.	geometry-based	2	2	2	5	10
d_T d_R	The spacing between two adjacent array elements at the Tx and Rx, respectively.	geometry-based	0, 0.5 λ, 1 λ 0, 0.5 λ, 1 λ	0, 0.5 λ, 1 λ 0, 0.5 λ, 1 λ	0, 1 λ, 2 λ 0, 1 λ, 2 λ	0 0	0 0.5 m
h [m] h_T [m] h_R [m]	The water depth, the Tx depth, and the Rx depth, respectively.	geometry-based	100 50 50	50 18 18	50 18 18	20 19 18	103 50 50
θ_T θ_R	The orientation of the Tx and Rx transducer array relative to the x-axis, respectively.	geometry-based	90° 90°	90° 90°	90° 90°	90° 90°	90° 90°
γ_T, γ_R	The moving directions of the Tx and Rx, in the x-z plane (relative to the x-axis), respectively.	geometry-based	90° 90°	40' 40'	90° 90°	90° 90°	90° 90°
c [m/s]	The speed of sound	geometry-based	1500	1500	1500	1470	1440
f_c [kHz]	The carrier frequency	geometry-based	1.7	10	17	17	1.2
v_T [m/s] v_R [m/s]	The velocities of the Tx and Rx, respectively.	geometry-based or estimated	0 0	2 2	0 0	0.0006 0.00025	0 0
K	The Rice factor	Estimated or selected to represent given propagation environment	0.6	0.6	0	0.8	0.71
$\zeta_{\Delta Z_{DA10}}$ $\zeta_{\Delta Z_{DA11}}$ $\zeta_{\Delta Z_{UA10}}$ $\zeta_{\Delta Z_{UA11}}$	The variances in the Gaussian pdf for the vertical displacements.	Estimated or selected to represent given propagation environment	0.1 0.1 0.1 0.1	0.09 0.09 0.09 0.09	0.1 0.1 0.1 0.1	0.0097 0.0097 0.0087 0.0087	0.019 0.019 0.015 0.015
μ_{DA10} μ_{DA11} μ_{UA10} μ_{UA11}	The mean AoAs.	Estimated or selected to represent given propagation environment	166' 163.5' 191.9' 192.9'	178' 177' 182' 183'	160' 157' 190' 191'	169' 167' 194' 195'	173.8' 173.4' 183' 184.5'
σ_{DA10} σ_{DA11} σ_{UA10} σ_{UA11}	The angle spreads for AoAs.	Estimated or selected to represent given propagation environment	2.5' 4' 2.4' 3'	10' 13.6' 10' 13.6'	2.55' 3.1' 4' 6'	3.25' 5' 2.7' 3.2'	9.1' 10.2' 5.59' 8.89'
η_S η_B	Specify how much the UA and DA rays contribute in the total averaged power, i.e., $\eta_S + \eta_B = 1$	Estimated or selected to represent given propagation environment	0.6 0.4	0.4 0.6	0.8 0.2	0.28 0.72	0.44 0.56

The results in Figs. 7 - 10 show good match between the measured and analytical data. This result illustrates the validity of the derived statistics and validates the estimation methods used to find the model parameters. Furthermore, the results in Figs. 7 and 8 show that both temporal and frequency correlation functions decay exponentially with Δt and Δf, respectively. Finally, in contrast to radio channels where signals de-correlate relatively fast, in SWA channels signals stay highly correlated. The reason for this behavior is the reduced amount of randomness in SWA channel. Note that macro-eigenrays are deterministic and only randomness is introduced by micro-eigenrays that have small variations around macro-eigenrays.

Finally, Fig. 11 compares the spatial correlation $R_{pq,\tilde{p}\tilde{q}}(0, 0)$ in (38) with the analytical spatial correlation in [12] and the analytical and empirical spatial correlations in [14]. The ASCOT01 channel measurements are collected at the carrier frequency 1.2 kHz and the speed of sound is $c = 1440$ m/s (i.e., λ=1.2 m) [14]. The distance between the $\mathrm{T_x}$ and $\mathrm{R_x}$ is $R = 10$ km. The water, $\mathrm{T_x}$, and $\mathrm{R_x}$ depths are $h = 103$ m, $h_T = 50$ m, and $h_R = 50$ m, respectively. The $\mathrm{R_x}$ is equipped with 33 vertically oriented transducer elements (i.e., $\theta_R = 90°$) with $L = d_R = 0.5$ m element spacing, while the $\mathrm{T_x}$ is equipped with one vertical transducer (i.e., $\theta_T = 90°$). The vertical correlation is calculated with respect to eighth element from the bottom of the 33-element array. The analytical spatial

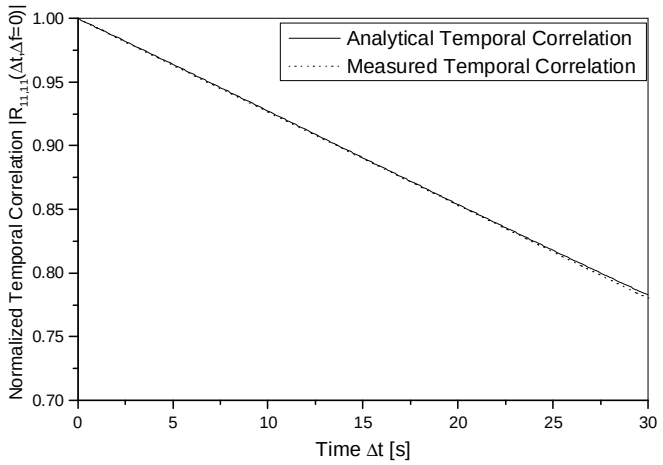

Fig. 7. The magnitudes of analytical and measured temporal correlation functions.

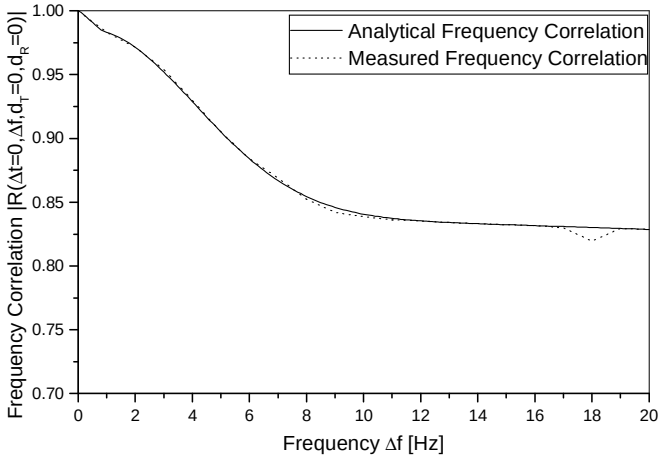

Fig. 8. The magnitudes of analytical and measured frequency correlation functions.

correlation in (38) is obtained with the estimated parameters $K = 0.71$, $S = B = 1$, $\mu_{DA10} = 173.8°$, $\mu_{DA11} = 173.4°$, $\mu_{UA10} = 183°$, $\mu_{UA11} = 184.5°$, $\sigma_{DA10} = 9.1°$, $\sigma_{DA11} = 10.2°$, $\sigma_{UA10} = 5.59°$, $\sigma_{UA11} = 8.89°$, $\eta_S = 0.44$, $\zeta_{\Delta Z_{DA10}} = \zeta_{\Delta Z_{DA11}} = 0.019$, $\zeta_{\Delta Z_{UA10}} = \zeta_{\Delta Z_{UA11}} = 0.015$, and $\eta_B = 1 - \eta_S$. The parameters R, h, h_T, h_R, θ_T, θ_R, and $\alpha_{TR} \approx \pi$, are selected to match the measurement conditions described above. The parameters used to obtain the curves in Fig. 11 are summarized in the eight column of Table II. For the reference, Fig. 11 also shows the spatial correlation functions of the exponential model in [14], i.e, $\exp\{-L^2/(2\lambda)^2\}$ and the particle-velocity model in [12] (with parameters $\Lambda_b = 0.56$, $\mu_b = 183°$, $\mu_s = 173°$, $\sigma_b = 2.29°$, and $\sigma_s = 8°$). One can observe that the proposed model provides a closer match with the experimental correlation than the models in [12] and [14]. Although the proposed model has a large number of parameters that can be adjusted, they are not the reason for an improved fidelity to experimental data. The exponential model in [14] fits an exponential function with distance between hydrophones as a parameter into the measured data. On the other hand, the particle-velocity model in [12] models a channel impulse response in SWA channel as a large number of random macro-eigenrays. However, this is unrealistic assumption because the experimental results show that the number of different macro-eigenrays that arrive at the receiver rarely exceeds eight [11], [14], [13]. In contrast, the proposed model characterizes SWA channel as a superposition of a LoS component and several macro-eigenrays, where each macro-eigenray is modeled as a large number of micro-eigenrays. This approach leads to a closer match with the experimental data. Note that a large number of parameters helps fine-tuning the model rather than fitting the model to any measured curve, as can be observed from Table II.

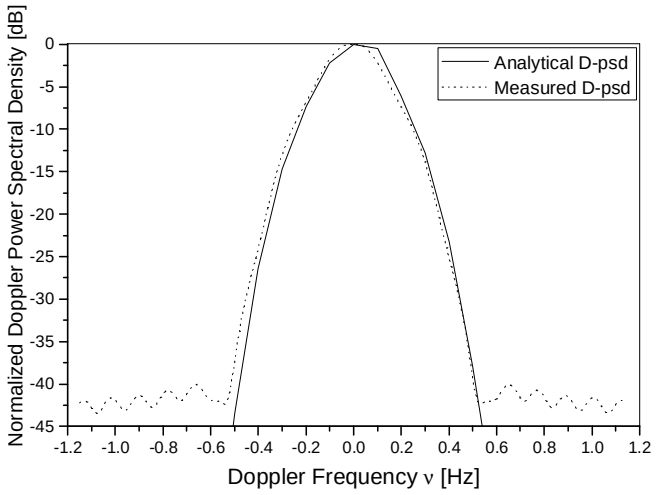

Fig. 9. The normalized analytical and measured Doppler power spectral density.

The close agreement between the analytical and measured statistics in Figs. 7 - 11 confirms the utility of the derived statistics. Here we note that the variance of vertical displacement and the means and variances of AoAs can be characterized as functions of sea state (i.e., water depth, seafloor roughness, etc.). However, this is not a straight forward task and is outside of the scope of this paper.

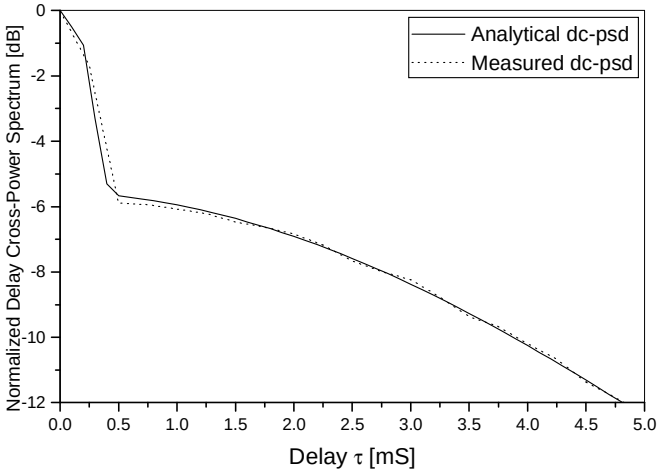

Fig. 10. The normalized analytical and measured delay cross-power spectral density.

V. Conclusions

This paper proposed the geometry-based statistical model for MIMO M-to-M SWA fading channels. From the statistical model, the corresponding MIMO time-frequency correlation function, Doppler power spectral density, and delay cross-power spectral density are derived and illustrated with several examples. Finally, the derived characteristics are compared with the experimentally obtained channel characteristics and the close agreement is observed. The main advantage of the proposed model is that it expresses the acoustic field correlation as a function of the angles of arrival and angle spreads. This allows system engineers to understand how these channel parameters affect the correlation, which in turn provides useful guidelines for the system design.

Acknowledgment

The author would like to thank the anonymous reviewers whose feedback helped improve the quality of this paper.

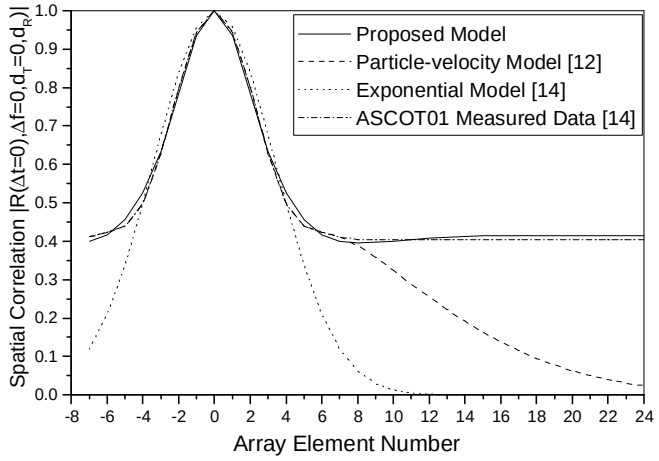

Fig. 11. Comparison of the analytical spatial correlations in (38), [12], and [14] with the measured spatial correlation in [14].

Appendix A
Derivations of Equations (15) - (19)

From Fig. 3, using the cosine law, the distances $\epsilon^{(p)}_{Ts\hat{b}n}$, $\epsilon^{(p)}_{Tb\hat{s}m}$, $\epsilon^{(q)}_{Rs\hat{b}n}$, $\epsilon^{(q)}_{Rb\hat{s}m}$, and ϵ_{pq} can be written as

$$\left(\epsilon^{(p)}_{Ts\hat{b}n}\right)^2 = \left[\frac{(L_t+1-2p)}{2}d_T\right]^2 + \left(\frac{h_T}{\sin(\pi-\alpha_{Rs\hat{b}n})}\right)^2 - \quad \text{(A.1)}$$
$$2\left(\frac{L_t+1-2p}{2}\right)d_T\left(\frac{h_T}{\sin(\pi-\alpha_{Rs\hat{b}n})}\right)\cos\left(\theta_T-\pi+\alpha_{Rs\hat{b}n}\right),$$

$$\left(\epsilon^{(p)}_{Tb\hat{s}m}\right)^2 = \left[\frac{(L_t+1-2p)}{2}d_T\right]^2 + \left(\frac{h-h_T}{\sin(\alpha_{Rb\hat{s}m}-\pi)}\right)^2 - \text{(A.2)}$$
$$2\left(\frac{L_t+1-2p}{2}\right)d_T\left(\frac{h-h_T}{\sin(\alpha_{Rb\hat{s}m}-\pi)}\right)\cos\left(\theta_T-\pi+\alpha_{Rb\hat{s}m}\right),$$

$$\left(\epsilon^{(q)}_{Rs\hat{b}n}\right)^2 = \left[\frac{(L_r+1-2q)}{2}d_R\right]^2 + \left(\frac{h_R}{\sin\alpha_{Rs\hat{b}n}}\right)^2 - \quad \text{(A.3)}$$
$$2\left(\frac{L_r+1-2q}{2}\right)d_R\left(\frac{h_R}{\sin\alpha_{Rs\hat{b}n}}\right)\cos\left(\alpha_{Rs\hat{b}n}-\theta_R\right),$$

$$\left(\epsilon^{(q)}_{Rb\hat{s}m}\right)^2 = \left[\frac{(L_r+1-2q)}{2}d_R\right]^2 + \left(\frac{h-h_R}{\sin(\alpha_{Rb\hat{s}m}-\pi)}\right)^2 \quad \text{(A.4)}$$
$$-2\left(\frac{L_r+1-2q}{2}\right)d_R\left(\frac{h-h_R}{\sin(\alpha_{Rb\hat{s}m}-\pi)}\right)\cos\left(\alpha_{Rb\hat{s}m}-\theta_R\right),$$

$$\epsilon^2_{pq} = \left[\frac{L_r+1-2q}{2}d_R\right]^2 + \epsilon^2 -$$
$$\frac{L_r+1-2q}{2}d_R\epsilon\cos\left(\alpha_{TR}-\theta_R\right), \quad \text{(A.5)}$$

where $\epsilon^2 = \left[(0.5L_t+0.5-p)d_T\right]^2 + \epsilon^2_{TR} - 2(0.5L_t+0.5-p)d_T\epsilon_{TR}\cos(\theta_T-\pi-\alpha_{TR})$, and $\epsilon^2_{TR} = R^2+(h_T-h_R)^2$. For small angle spreads, $d_T \ll \min(h_T, h-h_T)$, and $d_R \ll \min(h_R, h-h_R)$, we can use approximation $\sqrt{1+x} \approx 1 + x/2$, for small x to obtain the expressions in (15)-(19).

Appendix B
Derivation of the tf-cfs for UA and DA Components

Substituting (31) and (32) into (36) and (37), respectively, and noting that the phases $\phi_{b\hat{s}m}$ and $\phi_{s\hat{b}n}$ are independent and uniformly distributed over $[-\pi, \pi)$, the tf-cfs of UA and DA components can be written as

$$R^{UA}_{pq,\tilde{p}\tilde{q}}(t_1,f_1,t_2,f_2) = \frac{\eta_B}{2B}\sum_{b=1}^{B}\sum_{\hat{s}=b-1}^{b}\frac{1}{M_{b\hat{s}}}\sum_{m=1}^{M_{b\hat{s}}}\mathrm{E}[\xi^2_{b\hat{s}m}]$$
$$e^{-j\frac{2\pi(f_2-f_1)}{c}\left[\tilde{D}^{UA}_{b\hat{s}}-\frac{h_R+h_T-2h}{\sin\mu_{UAb\hat{s}}}+\frac{h_R+h_T-2h}{\sin\alpha_{Rb\hat{s}m}}\right]}$$
$$e^{j\frac{2\pi}{\lambda}[(p-\tilde{p})d_T\cos(\alpha_{Rb\hat{s}m}+\theta_T)-(q-\tilde{q})d_R\cos(\alpha_{Rb\hat{s}m}-\theta_R)]}$$
$$e^{j\frac{2\pi}{\lambda}[v_T(t_2-t_1)\cos(\alpha_{Rb\hat{s}m}+\gamma_T)-v_R(t_2-t_1)\cos(\alpha_{Rb\hat{s}m}-\gamma_R)]}$$
$$e^{j\frac{2\pi f_1}{c}[v_T(t_2-t_1)\cos(\alpha_{Rb\hat{s}m}+\gamma_T)-v_R(t_2-t_1)\cos(\alpha_{Rb\hat{s}m}-\gamma_R)]}$$
$$e^{j\frac{2\pi(f_2-f_1)}{c}[v_Tt_2\cos(\alpha_{Rb\hat{s}m}+\gamma_T)-v_Rt_2\cos(\alpha_{Rb\hat{s}m}-\gamma_R)]}$$
$$\mathrm{E}_{\Delta Z_{b\hat{s}m}(t)}\left[e^{-j\frac{2\pi(f_c+f_1)}{c}(\Delta Z_{b\hat{s}m}(t_2)-\Delta Z_{b\hat{s}m}(t_1))\sin\alpha_{Rb\hat{s}m}}\right.$$
$$\left.e^{-j\frac{2\pi(f_2-f_1)}{c}\Delta Z_{b\hat{s}m}(t_2)\sin\alpha_{Rb\hat{s}m}}\right], \quad \text{(B.1)}$$

$$R^{DA}_{pq,\tilde{p}\tilde{q}}(t_1,f_1,t_2,f_2) = \frac{\eta_S}{2S}\sum_{s=1}^{S}\sum_{\hat{b}=s-1}^{s}\frac{1}{N_{s\hat{b}}}\sum_{n=1}^{N_{s\hat{b}}}\mathrm{E}[\xi^2_{s\hat{b}n}]$$
$$e^{-j\frac{2\pi(f_2-f_1)}{c}\ \tilde{D}^{DA}_{s\hat{b}}-\frac{h_R+h_T}{\sin\mu_{DAs\hat{b}}}+\frac{h_R+h_T}{\sin\alpha_{Rs\hat{b}n}}}$$
$$e^{j\frac{2\pi}{\lambda}\left[(p-\tilde{p})d_T\cos(\alpha_{Rs\hat{b}n}+\theta_T)-(q-\tilde{q})d_R\cos(\alpha_{Rs\hat{b}n}-\theta_R)\right]}$$
$$e^{j\frac{2\pi}{\lambda}\left[v_T(t_2-t_1)\cos(\alpha_{Rs\hat{b}n}+\gamma_T)-v_R(t_2-t_1)\cos(\alpha_{Rs\hat{b}n}-\gamma_R)\right]}$$
$$e^{j\frac{2\pi f_1}{c}\left[v_T(t_2-t_1)\cos(\alpha_{Rs\hat{b}n}+\gamma_T)-v_R(t_2-t_1)\cos(\alpha_{Rs\hat{b}n}-\gamma_R)\right]}$$
$$e^{j\frac{2\pi(f_2-f_1)}{c}\left[v_Tt_2\cos(\alpha_{Rs\hat{b}n}+\gamma_T)-v_Rt_2\cos(\alpha_{Rs\hat{b}n}-\gamma_R)\right]}$$
$$\mathrm{E}_{\Delta Z_{s\hat{b}n}(t)}\left[e^{-j\frac{2\pi(f_c+f_1)}{c}(\Delta Z_{s\hat{b}n}(t_2)-\Delta Z_{s\hat{b}n}(t_1))\sin\alpha_{Rs\hat{b}n}}\right.$$
$$\left.e^{-j\frac{2\pi(f_2-f_1)}{c}\Delta Z_{s\hat{b}n}(t_2)\sin\alpha_{Rs\hat{b}n}}\right], \quad \text{(B.2)}$$

where $\mathrm{E}_{\Delta Z_{b\hat{s}m}(t)}[\cdot]$ and $\mathrm{E}_{\Delta Z_{s\hat{b}n}(t)}[\cdot]$ denote the statistical expectations with respect to $\Delta Z_{b\hat{s}m}(t)$ and $\Delta Z_{s\hat{b}n}(t)$, respectively.

The terms $\mathrm{E}[\xi^2_{b\hat{s}m}]/M_{b\hat{s}}$ and $\mathrm{E}[\xi^2_{s\hat{b}n}]/N_{s\hat{b}}$ in (B.1) and (B.2) represent the average powers received from the scatterers $S^{(B)}_{b\hat{s}m}$ and $S^{(S)}_{s\hat{b}n}$, respectively. Assuming that $\sum_{m=1}^{M_{b\hat{s}}}\mathrm{E}[\xi^2_{b\hat{s}m}]/M_{b\hat{s}} =$

1, $\sum_{n=1}^{N_{s\hat{b}}} \mathrm{E}[\xi^2_{s\hat{b}n}]/N_{s\hat{b}} = 1$, and the large number of micro-eigenrays, i.e., $M_{b\hat{s}} \gg 1$ and $N_{s\hat{b}} \gg 1$, the discrete AoAs, $\alpha_{Rb\hat{s}m}$ and $\alpha_{Rs\hat{b}n}$ can be replaced with continuous random variables $\alpha_{Rb\hat{s}}$ and $\alpha_{Rs\hat{b}}$ characterized with pdfs $f_{\text{bottom}}(\alpha_{Rb\hat{s}})$ and $f_{\text{top}}(\alpha_{Rs\hat{b}})$ respectively. Furthermore, the summations $\sum_{m=1}^{M_{b\hat{s}}}$ and $\sum_{n=1}^{N_{s\hat{b}}}$ in (B.1) and (B.2) can be replaced by integrals, i.e.,

$$
\begin{aligned}
&R^{UA}_{pq,\tilde{p}\tilde{q}}(t_1,f_1,t_2,f_2) = \frac{\eta_B}{2B}\sum_{b=1}^{B}\sum_{\hat{s}=b-1}^{b}\int_{\pi}^{2\pi} \\
&e^{-j\frac{2\pi(f_2-f_1)}{c}\left[\tilde{D}^{UA}_{b\hat{s}}-\frac{h_R+h_T-2h}{\sin\mu_{UAb\hat{s}}}+\frac{h_R+h_T-2h}{\sin\alpha_{Rb\hat{s}m}}\right]} \\
&e^{j\frac{2\pi}{\lambda}[(p-\tilde{p})d_T\cos(\alpha_{Rb\hat{s}m}+\theta_T)-(q-\tilde{q})d_R\cos(\alpha_{Rb\hat{s}m}-\theta_R)]} \\
&e^{j\frac{2\pi}{\lambda}[v_T(t_2-t_1)\cos(\alpha_{Rb\hat{s}m}+\gamma_T)-v_R(t_2-t_1)\cos(\alpha_{Rb\hat{s}m}-\gamma_R)]} \\
&e^{j\frac{2\pi f_1}{c}[v_T(t_2-t_1)\cos(\alpha_{Rb\hat{s}m}+\gamma_T)-v_R(t_2-t_1)\cos(\alpha_{Rb\hat{s}m}-\gamma_R)]} \\
&e^{j\frac{2\pi(f_2-f_1)}{c}[v_Tt_2\cos(\alpha_{Rb\hat{s}m}+\gamma_T)-v_Rt_2\cos(\alpha_{Rb\hat{s}m}-\gamma_R)]} \\
&\mathrm{E}_{\Delta Z_{b\hat{s}m}(t)}\Bigg[e^{-j\frac{2\pi(f_c+f_1)}{c}(\Delta Z_{b\hat{s}m}(t_2)-\Delta Z_{b\hat{s}m}(t_1))\sin\alpha_{Rb\hat{s}m}} \\
&e^{-j\frac{2\pi(f_2-f_1)}{c}\Delta Z_{b\hat{s}m}(t_2)\sin\alpha_{Rb\hat{s}m}}\Bigg]d\alpha_{Rb\hat{s}}, \qquad \text{(B.3)}
\end{aligned}
$$

$$
\begin{aligned}
&R^{DA}_{pq,\tilde{p}\tilde{q}}(t_1,f_1,t_2,f_2) = \frac{\eta_S}{2S}\sum_{s=1}^{S}\sum_{\hat{b}=s-1}^{s}\int_{0}^{\pi} \\
&e^{-j\frac{2\pi(f_2-f_1)}{c}\left[\tilde{D}^{DA}_{s\hat{b}}-\frac{h_R+h_T}{\sin\mu_{DAs\hat{b}}}+\frac{h_R+h_T}{\sin\alpha_{Rs\hat{b}n}}\right]} \\
&e^{j\frac{2\pi}{\lambda}\left[(p-\tilde{p})d_T\cos(\alpha_{Rs\hat{b}n}+\theta_T)-(q-\tilde{q})d_R\cos(\alpha_{Rs\hat{b}n}-\theta_R)\right]} \\
&e^{j\frac{2\pi}{\lambda}\left[v_T(t_2-t_1)\cos(\alpha_{Rs\hat{b}n}+\gamma_T)-v_R(t_2-t_1)\cos(\alpha_{Rs\hat{b}n}-\gamma_R)\right]} \\
&e^{j\frac{2\pi f_1}{c}\left[v_T(t_2-t_1)\cos(\alpha_{Rs\hat{b}n}+\gamma_T)-v_R(t_2-t_1)\cos(\alpha_{Rs\hat{b}n}-\gamma_R)\right]} \\
&e^{j\frac{2\pi(f_2-f_1)}{c}\left[v_Tt_2\cos(\alpha_{Rs\hat{b}n}+\gamma_T)-v_Rt_2\cos(\alpha_{Rs\hat{b}n}-\gamma_R)\right]} \\
&\mathrm{E}_{\Delta Z_{s\hat{b}n}(t)}\Bigg[e^{-j\frac{2\pi(f_c+f_1)}{c}(\Delta Z_{s\hat{b}n}(t_2)-\Delta Z_{s\hat{b}n}(t_1))\sin\alpha_{Rs\hat{b}n}} \\
&e^{-j\frac{2\pi(f_2-f_1)}{c}\Delta Z_{s\hat{b}n}(t_2)\sin\alpha_{Rs\hat{b}n}}\Bigg]d\alpha_{Rs\hat{b}}, \qquad \text{(B.4)}
\end{aligned}
$$

Since $\Delta Z_{b\hat{s}}(t)$ has stationary and independent increments with pdf defined in (28), the expectation $\mathrm{E}_{\Delta Z_{b\hat{s}}(t)}[\cdot]$ in (B.3) can be calculated as follows

$$
\begin{aligned}
&\int_{-\infty}^{\infty} e^{-j\frac{2\pi(f_c+f_1)}{c}(\Delta Z_{b\hat{s}}(t_2)-\Delta Z_{b\hat{s}}(t_1))\sin\alpha_{Rb\hat{s}}} \qquad \text{(B.5)} \\
&f(\Delta Z_{b\hat{s}}(t_2)-\Delta Z_{b\hat{s}}(t_1))d(\Delta Z_{b\hat{s}}(t_2)-\Delta Z_{b\hat{s}}(t_1)) \\
&\int_{-\infty}^{\infty} e^{-j\frac{2\pi}{c}\sin\alpha_{Rb\hat{s}}(f_2-f_1)\Delta Z_{b\hat{s}}(t_2)}f(\Delta Z_{b\hat{s}}(t_2))d(\Delta Z_{b\hat{s}}(t_2)) = \\
&\exp\Bigg\{-\frac{(t_2-t_1)\zeta^2_{\Delta Z_{UAb\hat{s}}}}{2}\left[\frac{2\pi(f_c+f_1)}{c}\sin\alpha_{Rb\hat{s}}\right]^2- \\
&\frac{t_2\zeta^2_{\Delta Z_{UAb\hat{s}}}}{2}\left[\frac{2\pi(f_2-f_1)}{c}\sin\alpha_{Rb\hat{s}}\right]^2\Bigg\}.
\end{aligned}
$$

Similarly, the expectation $\mathrm{E}_{\Delta Z_{s\hat{b}}(t)}[\cdot]$ in (B.4) becomes

$$
\begin{aligned}
&\exp\Bigg\{-\frac{(t_2-t_1)\zeta^2_{\Delta Z_{DAs\hat{b}}}}{2}\left[\frac{2\pi(f_c+f_1)}{c}\sin\alpha_{Rs\hat{b}}\right]^2- \\
&\frac{t_2\zeta^2_{\Delta Z_{DAs\hat{b}}}}{2}\left[\frac{2\pi(f_2-f_1)}{c}\sin\alpha_{Rs\hat{b}}\right]^2\Bigg\}.
\end{aligned}
$$

Substituting (B.5) and (26) into (B.3) and (B.6) and (25) into (B.4), we obtain the following expressions for the tf-cfs of the UA and DA components, respectively,

$$
\begin{aligned}
&R^{UA}_{pq,\tilde{p}\tilde{q}}(t_1,f_1,t_2,f_2) = \frac{\eta_B}{2B}\sum_{b=1}^{B}\sum_{\hat{s}=b-1}^{b}\int_{\pi}^{2\pi}\frac{1}{\sqrt{2\pi\sigma^2_{UAb\hat{s}}}} \qquad \text{(B.6)} \\
&e^{-\frac{(\alpha_{Rb\hat{s}}-\mu_{UAb\hat{s}})^2}{(2\sigma^2_{UAb\hat{s}})}-j\frac{2\pi(f_2-f_1)}{c}\left[\tilde{D}^{UA}_{b\hat{s}}-\frac{h_R+h_T-2h}{\sin\mu_{UAb\hat{s}}}+\frac{h_R+h_T-2h}{\sin\alpha_{Rb\hat{s}}}\right]} \\
&e^{j\frac{2\pi f_c}{c}[(p-\tilde{p})d_T\cos(\alpha_{Rb\hat{s}}+\theta_T)-(q-\tilde{q})d_R\cos(\alpha_{Rb\hat{s}}-\theta_R)]} \\
&e^{j\frac{2\pi f_c}{c}[v_T(t_2-t_1)\cos(\alpha_{Rb\hat{s}}+\gamma_T)-v_R(t_2-t_1)\cos(\alpha_{Rb\hat{s}}-\gamma_R)]} \\
&e^{j\frac{2\pi f_1}{c}[v_T(t_2-t_1)\cos(\alpha_{Rb\hat{s}}+\gamma_T)-v_R(t_2-t_1)\cos(\alpha_{Rb\hat{s}}-\gamma_R)]} \\
&e^{j\frac{2\pi(f_2-f_1)}{c}[v_Tt_2\cos(\alpha_{Rb\hat{s}}+\gamma_T)-v_Rt_2\cos(\alpha_{Rb\hat{s}}-\gamma_R)]} \\
&e^{-\frac{(t_2-t_1)\zeta^2_{\Delta Z_{UAb\hat{s}}}}{2}\left[\frac{2\pi(f_c+f_1)}{c}\sin\alpha_{Rb\hat{s}}\right]^2} \\
&e^{-\frac{t_2\zeta^2_{\Delta Z_{UAb\hat{s}}}}{2}\left[\frac{2\pi(f_2-f_1)}{c}\sin\alpha_{Rb\hat{s}}\right]^2}d\alpha_{Rb\hat{s}},
\end{aligned}
$$

$$
\begin{aligned}
&R^{DA}_{pq,\tilde{p}\tilde{q}}(t_1,f_1,t_2,f_2) = \frac{\eta_S}{2S}\sum_{s=1}^{S}\sum_{\hat{b}=s-1}^{s}\int_{0}^{\pi}\frac{1}{\sqrt{2\pi\sigma^2_{DAs\hat{b}}}} \qquad \text{(B.7)} \\
&e^{-\frac{(\alpha_{Rs\hat{b}}-\mu_{DAs\hat{b}})^2}{(2\sigma^2_{DAs\hat{b}})}}e^{-j\frac{2\pi(f_2-f_1)}{c}\left[\tilde{D}^{DA}_{s\hat{b}}-\frac{h_R+h_T}{\sin\mu_{DAs\hat{b}}}+\frac{h_R+h_T}{\sin\alpha_{Rs\hat{b}}}\right]} \\
&e^{j\frac{2\pi f_c}{c}\left[(p-\tilde{p})d_T\cos(\alpha_{Rs\hat{b}}+\theta_T)-(q-\tilde{q})d_R\cos(\alpha_{Rs\hat{b}}-\theta_R)\right]} \\
&e^{j\frac{2\pi f_c}{c}\left[v_T(t_2-t_1)\cos(\alpha_{Rs\hat{b}}+\gamma_T)-v_R(t_2-t_1)\cos(\alpha_{Rs\hat{b}}-\gamma_R)\right]} \\
&e^{j\frac{2\pi f_1}{c}\left[v_T(t_2-t_1)\cos(\alpha_{Rs\hat{b}}+\gamma_T)-v_R(t_2-t_1)\cos(\alpha_{Rs\hat{b}}-\gamma_R)\right]} \\
&e^{j\frac{2\pi(f_2-f_1)}{c}\left[v_Tt_2\cos(\alpha_{Rs\hat{b}}+\gamma_T)-v_Rt_2\cos(\alpha_{Rs\hat{b}}-\gamma_R)\right]} \\
&e^{-\frac{(t_2-t_1)\zeta^2_{\Delta Z_{DAs\hat{b}}}}{2}\left[\frac{2\pi(f_c+f_1)}{c}\sin\alpha_{Rs\hat{b}}\right]^2} \\
&e^{-\frac{t_2\zeta^2_{\Delta Z_{DAs\hat{b}}}}{2}\left[\frac{2\pi(f_2-f_1)}{c}\sin\alpha_{Rs\hat{b}}\right]^2}d\alpha_{Rs\hat{b}}.
\end{aligned}
$$

For small angle spreads, the AoAs $\alpha_{Rs\hat{b}}$ and $\alpha_{Rb\hat{s}}$ are mainly concentrated around the mean AoAs $\mu_{DAs\hat{b}}$ and $\mu_{UAb\hat{s}}$, respectively. Using the first-order Taylor expansion, the AoA angles can be approximated as follows

$$
\begin{aligned}
&\cos(\alpha_{Rs\hat{b}}) \approx \cos(\mu_{DAs\hat{b}}) - \sin(\mu_{DAs\hat{b}})(\alpha_{Rs\hat{b}}-\mu_{DAs\hat{b}}) \qquad \text{(B.8)} \\
&\sin(\alpha_{Rs\hat{b}}) \approx \sin(\mu_{DAs\hat{b}}) + \cos(\mu_{DAs\hat{b}})(\alpha_{Rs\hat{b}}-\mu_{DAs\hat{b}}) \qquad \text{(B.9)} \\
&\sin(\alpha_{Rs\hat{b}})^2 \approx \sin(\mu_{DAs\hat{b}})^2 + 2\sin(\mu_{DAs\hat{b}})\cos(\mu_{DAs\hat{b}}) \\
&(\alpha_{Rs\hat{b}}-\mu_{DAs\hat{b}}) \qquad \text{(B.10)} \\
&\sin(\alpha_{Rs\hat{b}})^{-1} \approx \sin(\mu_{DAs\hat{b}})^{-1} - \cos(\mu_{DAs\hat{b}}) \\
&(\alpha_{Rs\hat{b}}-\mu_{DAs\hat{b}})/\sin(\mu_{DAs\hat{b}})^{-2}. \qquad \text{(B.11)}
\end{aligned}
$$

The similar approximations are applied to the AoAs $\alpha_{Rb\hat{s}}$. Using these trigonometric approximations and the equality $\int e^{j\alpha x}(2\pi\sigma^2)^{-1/2}e^{-x^2/(2\sigma^2)}dx = e^{-\sigma^2\alpha^2/2}$ [12], the tf-cfs of the UA and DA components can be written as in (41) and (42), respectively.

Appendix C
The D-psd of the UA and DA Components

The Fourier transforms of the time-frequency correlation functions $R^{UA}_{pq,\tilde{p}\tilde{q}}(\Delta t,\Delta f=0)$ and $R^{DA}_{pq,\tilde{p}\tilde{q}}(\Delta t,\Delta f=0)$ can

be written as

$$S^{UA}_{pq,\tilde{p}\tilde{q}}(\nu) = \frac{\eta_B}{2B}\sum_{b=1}^{B}\sum_{\hat{s}=b-1}^{b} \tag{C.1}$$

$$e^{j\frac{2\pi}{\lambda}[(p-\tilde{p})d_T\cos(\mu_{UAb\hat{s}}+\theta_T)-(q-\tilde{q})d_R\cos(\mu_{UAb\hat{s}}-\theta_R)]}\int_{-\infty}^{\infty}$$

$$\exp\left\{-\frac{\sigma^2_{UAb\hat{s}}}{2}\left[\Delta t\zeta^2_{\Delta Z_{UAb\hat{s}}}\left[\frac{2\pi}{\lambda}\right]^2\sin\mu_{UAb\hat{s}}\cos\mu_{UAb\hat{s}}+\frac{2\pi}{\lambda}\right.\right.$$

$$(q-\tilde{q})d_R\sin(\mu_{UAb\hat{s}}-\theta_R)+v_R\Delta t\sin(\mu_{UAb\hat{s}}-\gamma_R)-\frac{2\pi}{\lambda}$$

$$\left.\left.[(p-\tilde{p})d_T\sin(\mu_{UAb\hat{s}}+\theta_T)-v_T\Delta t\sin(\mu_{UAb\hat{s}}+\gamma_T)]\right]^2\right\}$$

$$e^{-j2\pi\nu\Delta t-\frac{\Delta t\zeta^2_{\Delta Z_{UAb\hat{s}}}}{2}\left[\frac{2\pi}{\lambda}\sin\mu_{UAb\hat{s}}\right]^2}$$

$$e^{-j\frac{2\pi}{\lambda}[v_R\Delta t\cos(\mu_{UAb\hat{s}}-\gamma_R)-v_T\Delta t\cos(\mu_{UAb\hat{s}}+\gamma_T)]}d\Delta t,$$

$$S^{DA}_{pq,\tilde{p}\tilde{q}}(\nu) = \frac{\eta_S}{2S}\sum_{s=1}^{S}\sum_{\hat{b}=s-1}^{s} \tag{C.2}$$

$$e^{j\frac{2\pi}{\lambda}\left[(p-\tilde{p})d_T\cos(\mu_{DAs\hat{b}}+\theta_T)-(q-\tilde{q})d_R\cos(\mu_{DAs\hat{b}}-\theta_R)\right]}\int_{-\infty}^{\infty}$$

$$\exp\left\{-\frac{\sigma^2_{DAs\hat{b}}}{2}\left[\Delta t\zeta^2_{\Delta Z_{DAs\hat{b}}}\left[\frac{2\pi}{\lambda}\right]^2\sin\mu_{DAs\hat{b}}\cos\mu_{DAs\hat{b}}+\frac{2\pi}{\lambda}\right.\right.$$

$$(q-\tilde{q})d_R\sin(\mu_{DAs\hat{b}}-\theta_R)+v_R\Delta t\sin(\mu_{DAs\hat{b}}-\gamma_R)-\frac{2\pi}{\lambda}$$

$$\left.\left.\left[(p-\tilde{p})d_T\sin(\mu_{DAs\hat{b}}+\theta_T)-v_T\Delta t\sin(\mu_{DAs\hat{b}}+\gamma_T)\right]\right]^2\right\}$$

$$e^{-j2\pi\nu\Delta t-\frac{\Delta t\zeta^2_{\Delta Z_{DAs\hat{b}}}}{2}\left[\frac{2\pi}{\lambda}\sin\mu_{DAs\hat{b}}\right]^2}$$

$$e^{-j\frac{2\pi}{\lambda}\left[v_R\Delta t\cos(\mu_{DAs\hat{b}}-\gamma_R)-v_T\Delta t\cos(\mu_{DAs\hat{b}}+\gamma_T)\right]}d\Delta t.$$

Using the equality $\int_{-\infty}^{\infty}e^{-p^2x^2\pm qx}dx = \sqrt{\pi}e^{q^2/(4p^2)}/p$ [19, eq. 3.323-2] to solve the integrals in (C.1) and (C.2), we obtain the D-psds in (47) and (48).

REFERENCES

[1] M. Stojanovic, "Recent advances in high-speed underwater acoustic communications," *IEEE Journal of Oceanic Eng.*, vol. 21, pp. 125–136, Apr. 1996.

[2] B. J. Davis, P. T. Gough, B. R. Hunt, "Modeling surface multipath effects in synthetic aperture sonar," *IEEE Journal of Oceanic Eng.*, vol. 34, pp. 239–249, July 2009.

[3] T. E. Giddings, J. J. Shirron, "A model for sonar interrogation of complex bottom and surface targets in shallow-water waveguides," *Journal of the Acoustical Society of America*, vol. 123 pp. 2024–2034, Apr. 2008.

[4] T. B. Aik, Q. S. Sen, and Z. Nan, "Characterization of multipath acoustic channels in very shallow waters for communications," *Proc. OCEANS'06 Asia-Pacific*, Singapore, May 2007.

[5] M. Badiey, Y. Mu, J. A. Simmen, and S. E. Forsythe, "Signal variability in shallow-water sound channels," *IEEE Journal of Oceanic Eng.*, vol. 25, pp. 492–500, Oct. 2000.

[6] D. B. Kilfoyle and A. B. Baggeroer, "The state of the art in underwater acoustic telemetry," *IEEE Journal of Oceanic Eng.*, vol. 25, pp. 4–27, Jan. 2000.

[7] R. H. Owen, B. V. Smith, and R. F. W. Coates, "An experimental study of rough surface scattering and its effects on communication coherence," *Proc. OCEANS'94*, vol. 3, pp. 483–488, Brest, France, Sept. 1994.

[8] A. Essebbar, G. Loubet, and F. Vial, "Underwater acoustic channel simulations for communication," *Proc. OCEANS'94*, vol. 3, pp. 495–500, Brest, France, Sept. 1994.

[9] A. Zielinski, Y-H. Yoon, and L. Wu, "Performance analysis of digital acoustic communication in a shallow water channel," *IEEE Journal of Oceanic Eng.*, vol. 20, pp. 293–299, Oct. 1995.

[10] C. Bjerrum-Niese, L. Bjorno, M. A. Pinto, and B. Quellec, "A simulation tool for high data-rate acoustic communication in a shallow-water, time-varying channel," *IEEE Journal of Oceanic Eng.*, vol. 21, pp. 143–149, Apr. 1996.

[11] M. Chitre, "A high-frequency warm shallow water acoustic communications channel model and measurements," *J. Acoust. Soc. Am.*, vol. 122, pp. 2580–2586, Nov. 2007.

[12] A. Abdi and H. Guo, "Signal correlation modeling in acoustic vector sensor arrays," *IEEE Transactions on Signal Processing*, vol. 57, pp. 892–903, Mar. 2009.

[13] T. C. Yang, "Toward continuous underwater acoustic communications,"*Proc. OCEANS'08*, Quebec City, Canada, Sept. 2008.

[14] T. C. Yang, "A study of spatial processing gain in underwater acoustic communications," *IEEE Journal of Oceanic Eng.*, vol. 32, pp. 689–709, July 2007.

[15] L. M. Brekhovskikh and Y. Lysanov, *Fundamentals of ocean acoustics 2e*. Springer, Berlin, 1991.

[16] W. C. Jakes, *Microwave Mobile Communications*, 2nd ed. Piscataway, NJ: Wiley-IEEE Press, 1994.

[17] G. L. Stüber, *Principles of mobile communication 2e.*Kluwer, 2001.

[18] R. Kattenbach, "Statistical modeling of small-scale fading in directional radio channels," *Journal on Selected Area in Communications*, vol. 20, pp. 584–592, April 2002.

[19] I. S. Gradshteyn and I. M. Ryzhik, *Table of Integrals, Series, and Products* . San Diego, CA, 5th ed., 1994.

[20] L. J. Greenstein, D. G. Michelson, and V. Erceg, "Moment-method estimation of the Ricean K-factor," *IEEE Commun. Letters*, vol. 3, pp. 175–176, June 1999.

[21] A. G. Zajić, G. L. Stüber, T. G. Pratt, and S. Nguyen, "Wideband mimo mobile-to-mobile channels: geometry-based statistical modeling with experimental verification," *IEEE Trans. Veh. Tech.*, vol. 58, pp. 517-534, Feb. 2009.

[22] R. Fletcher, *Practical Methods of Optimization - Constrained Optimization 2e.*. John Wiley and Sons, 1981.

Alenka G. Zajić (S'99-M'08) received her B.Sc. and M.Sc. degrees from the School of Electrical Engineering, University of Belgrade, in 2001 and 2003, respectively. She received her Ph.D. degree in Electrical and Computer Engineering from the Georgia Institute of Technology in 2008. In 2010, she joined the School of Computer Science, Georgia Institute of Technology, where is visiting assistant professor. Her research interests are in wireless communications and applied electromagnetics.

Dr. Zajić received the Best Paper Award at ICT 2008, the Best Student Paper Award at WCNC 2007, and was also the recipient of the Dan Noble Fellowship in 2004, awarded by Motorola Inc. and IEEE Vehicular Technology Society for quality impact in the area of vehicular technology.